

Precession of magnetars: dynamical evolutions and modulations on polarized electromagnetic waves

Yong Gao,^{1,2} Lijing Shao,^{2,3,4}★ Gregory Desvignes,^{3,5} David Ian Jones,⁶ Michael Kramer,^{3,7} and Garvin Yim^{2,6}

¹*Department of Astronomy, School of Physics, Peking University, Beijing 100871, China*

²*Kavli Institute for Astronomy and Astrophysics, Peking University, Beijing 100871, China*

³*Max-Planck-Institut für Radioastronomie, Auf dem Hügel 69, D-53121 Bonn, Germany*

⁴*National Astronomical Observatories, Chinese Academy of Sciences, Beijing 100012, China*

⁵*Laboratoire d'Études Spatiales et d'Instrumentation en Astrophysique, Observatoire de Paris, Université Paris-Sciences-et-Lettres, Centre National de la Recherche Scientifique, Sorbonne Université, Université de Paris, 5 place Jules Janssen, 92195 Meudon, France*

⁶*Mathematical Sciences and STAG Research Centre, University of Southampton, Southampton SO17 1BJ, UK*

⁷*Jodrell Bank Centre for Astrophysics, School of Physics and Astronomy, The University of Manchester, Manchester M13 9PL, UK*

Accepted XXX. Received YYY; in original form ZZZ

ABSTRACT

Magnetars are conjectured to be highly magnetized neutron stars (NSs). Strong internal magnetic field and elasticity in the crust may deform the stars and lead to free precession. We study the precession dynamics of triaxially-deformed NSs incorporating the near-field and the far-field electromagnetic torques. We obtain timing residuals for different NS geometries and torques. We also investigate the polarized X-ray and radio signals from precessing magnetars. The modulations on the Stokes parameters are obtained for thermal X-rays emitted from the surface of magnetars. For radio signals, we apply the simple rotating vector model (RVM) to give the modulations on the position angle (PA) of the polarization. Our results are comprehensive, ready to be used to search for magnetar precession with timing data and polarizations of X-ray and radio emissions. Future observations of precessing magnetars will give us valuable information on the geometry and the strength of the strong magnetic fields, the emission geometry, as well as the equation of state (EoS) of NSs.

Key words: stars: magnetars – methods: analytical – X-rays: general – polarization

1 INTRODUCTION

The free precession of neutron stars (NSs) has been studied since the discovery of radio pulsars. The wobbling motion caused by the free precession is closely related to the structure of NSs, such as the elasticity in the crust (Ushomirsky et al. 2000; Cutler et al. 2003), the strength and the geometry of the internal and external magnetic fields (Haskell et al. 2008; Mastrano et al. 2013), the superfluid and superconducting states of the fluid interior (Pines 1974; Shaham 1977; Sedrakian et al. 1998; Link 2007; Glampedakis et al. 2008), as well as the evolution of the magnetic inclination angle (Mestel & Takhar 1972; Goldreich 1970; Melatos 2000; Lander & Jones 2018, 2020).

Although many theoretical works were devoted to this field, free precession has not been firmly observed yet. The most probable evidence of free precession comes from the radio pulsar PSR B1828–11, which shows highly periodical variations in the pulse phase over a period of ~ 500 d, accompanied by correlated changes in the beam width of pulses (Stairs et al. 2000). The data can be well fitted by the free precession model with the precession-modulated spin-down torque (Jones & Andersson 2001; Link & Epstein 2001; Akgun et al. 2006). Meanwhile, radio observations started to show that several pulsars, with harmonic features in their timing residuals, including

PSR B1828–11, undergo sudden sharp changes in pulse profiles which, at least for PSR B1931+24, correlates with sharp changes in spin-down torque (Kramer et al. 2006; Lyne et al. 2010; Shaw et al. 2022). Lyne et al. (2010) argued that the radio emissions switch back and forth between two different magnetospheric states, which leads to the harmonic timing residuals and changes in the pulse shape. The sharpness of the transitions is thought as strong evidence that free precession is not a viable mechanism to explain the harmonic timing residuals in PSR B1828–11. Further analysis by Stairs et al. (2019) also disfavored the free precession scenario. Mode switching is very appealing and reasonable to explain the harmonic timing data and shape variations, but the physics behind the sharp changes and the regular clock of the transitions needs more development. Jones (2012) provided an argument as to why abrupt magnetospheric changes can occur in precessing stars. In this regard, the free precession of PSR B1828–11 cannot be ruled out firmly yet (Ashton et al. 2016, 2017).

Different from normal pulsars, magnetars are a class of young NSs with strong magnetic fields, typically above 10^{14} G, and long spin periods, typically 2–10 s (Kaspi & Beloborodov 2017). The strong internal magnetic fields may distort the star (Melatos 1997, 2000). Due to the young age and energetic processes, the star may also develop large elastic deformation in the crust. Glitches or crust fracture may excite wobble angles and set the deformed magnetars into free precession. Strong magnetic fields also indicate large external elec-

★ E-mail: lshao@pku.edu.cn (LS)

tromagnetic torques, which include the far-field torque dissipating the kinetic energy and the near-field torque originating from the moment of inertia of the electromagnetic field itself (Goldreich 1970; Good & Ng 1985; Melatos 1997). The forced precession can be significant for magnetars due to their strong electromagnetic torques, but this effect would not affect the free precession if the object has even stronger internal magnetic fields reaching 10^{16} G (Makishima et al. 2014). We will investigate both free and forced precession in this work.

Early observations of timing irregularities of magnetars motivated Melatos (1997) to suggest that precession is common in AXP populations. However, further observations from X-ray timing in the band $\sim 1\text{--}10$ keV have ruled out precession at an amplitude level above the root-mean-square amplitude of timing noise (Kaspi et al. 1999, 2001). Small-amplitude precession that is buried in the timing noise of magnetars is still possible. Possible evidence of magnetar precession were found by the combined timing analysis of the hard and soft X-rays from three magnetars, 4U 0142+61 (Makishima et al. 2014), 1E 1547.0–5408 (Makishima et al. 2021a), and SGR 1900+14 (Makishima et al. 2021b). The phase modulations of hard X-ray are observed in those magnetars, which may indicate large magnetic deformations on the order of $\sim 10^{-4}$ (Makishima et al. 2014, 2021a,b). Recently, the precession of magnetars was also used to interpret the possible periodicity found in fast radio bursts (FRBs; Levin et al. 2020; Zanazzi & Lai 2020; Wasserman et al. 2022).

All above evidences of magnetar precession come from the timing residuals, where the rotation phase is modulated by precession. During the precession, the body itself also precesses around the deformation axis, which leads to the swing of the emission region. The polarization directly maps the emission geometry. Thus it is also promising to reveal precession from the variations of polarizations.

The soft component of the X-ray emission ($\sim 1\text{--}10$ keV) of magnetars is usually interpreted as thermal emission from the magnetar surface, which is reprocessed by the strongly magnetized atmosphere (Thompson et al. 2002; Turolla et al. 2015). Numerous studies have been dedicated to investigate the opacities and radiative transfer in strongly magnetized atmospheres, showing that the surface emission could be highly polarized (Meszaros 1992; Pavlov & Zavlin 2000; Ho & Lai 2003; Lai & Ho 2003; Taverna et al. 2015). Recently, the IXPE observation of 4U 0142+61 gave the first ever measurement of polarized emission from a magnetar in the soft X-ray band (Taverna et al. 2022). The observations provided us completely new information about the NS surface and magnetosphere and showed some evidence of vacuum birefringence in a strong magnetic field.

The radio emissions from magnetars are only observed in transient magnetars after energetic bursts and the signal itself is also transient (Camilo et al. 2006, 2007; Levin et al. 2010; Eatough et al. 2013; Lower et al. 2020). The emission is highly polarized. By applying the rotating vector model (RVM; Radhakrishnan & Cooke 1969), useful information was obtained on the magnetic field geometry of magnetars (Kramer et al. 2007; Levin et al. 2012; Lower et al. 2021).

In this paper, we aim to systematically study the dynamics of precessing magnetars and model the observational consequences in timing and polarization of electromagnetic waves. The structure of the paper is organized as follows. In Sec. 2, we discuss the possible deformation of magnetars. The free and forced precession dynamics of general triaxially-deformed magnetars are studied in Sec. 3. We give the phase modulations and timing residuals due to precession in Sec. 4. The modulations on polarized X-ray and radio signals are investigated in Sec. 5. We give discussions and conclusions in Sec. 6 and Sec. 7 respectively.

2 DEFORMATION OF MAGNETARS

To make the body precess, NSs must have some deformation misaligned with the rotational bulge. The strains in the solid crust and the strong internal magnetic fields are usually considered as potential causes of the deformation. In the following, we consider the possible sources of deformation. In the body frame, we can write the moment of inertia tensor of a slowly rotating NS as (Jones & Andersson 2001; Wasserman et al. 2022)

$$I_{ij} = I_0 \left[\delta_{ij} + \epsilon_{\text{rot}} \left(\frac{1}{3} \delta_{ij} - \hat{\omega}_i \hat{\omega}_j \right) + M_{ij} \right]. \quad (1)$$

Here I_0 is the spherical part of the moment of inertia. The rotational deformation is quadrupolar that is symmetric about the spin axis $\hat{\omega}$. We let ϵ_{rot} denote the ellipticity sourced from the centrifugal force, while the magnetic and elastic deformations are not necessarily axisymmetric. Thus, we use the symmetric and trace free (STF) tensor M_{ij} to describe the deformations sourced from the internal magnetic field, elasticity in the crust, or the combination of both.

For magnetars, the spin period P is on the order of several seconds and ϵ_{rot} can be approximated as the rotational energy over the gravitational energy

$$\epsilon_{\text{rot}} \approx \frac{\omega^2 R^3}{GM} = 8.5 \times 10^{-9} P_5^{-2} R_6^3 / M_{1.4}, \quad (2)$$

where $\omega = 2\pi/P$ is the spin angular frequency, P_5 is the spin period in units of 5 s, R_6 is the NS radius R in units of 10^6 cm, and $M_{1.4}$ is the NS mass M in units of $1.4 M_\odot$. The centrifugal deformation is of no importance for free precession (Glampedakis & Jones 2010; Wasserman et al. 2022), which can be understood as follows. The angular momentum for a freely-precessing NS can be written as

$$L_i = I_0 \left[\left(1 - \frac{2\epsilon_{\text{rot}}}{3} \right) \delta_{ij} \omega_j + M_{ij} \omega_j \right] = I'_0 \left(\delta_{ij} + M'_{ij} \right) \omega_j, \quad (3)$$

where Einstein summation is used, $I'_0 = I_0(1 - 2\epsilon_{\text{rot}}/3)$, and $M'_{ij} = M_{ij}/(1 - 2\epsilon_{\text{rot}}/3)$. Since the rotational ellipticity ϵ_{rot} is quite small, we can absorb the rotational bulges into the spherical part and approximately rewrite the moment of inertia tensor as

$$I_{ij} \simeq I_0 (\delta_{ij} + M_{ij}). \quad (4)$$

We let \hat{e}_1 , \hat{e}_2 , and \hat{e}_3 denote the three unit eigenvectors along the principal axes of moment of inertia tensor I_{ij} with corresponding eigenvalues $I_1 \leq I_2 \leq I_3$. The angular velocity is $\omega = \omega_1 \hat{e}_1 + \omega_2 \hat{e}_2 + \omega_3 \hat{e}_3$ and the angular momentum is $\mathbf{L} = L_1 \hat{e}_1 + L_2 \hat{e}_2 + L_3 \hat{e}_3$. To describe the motion of the body, we define

$$\begin{aligned} \epsilon &\equiv \frac{I_3 - I_1}{I_1}, \\ \delta &\equiv \frac{I_3(I_2 - I_1)}{I_1(I_3 - I_2)}, \\ \theta &\equiv \arccos \frac{L_3}{L}, \end{aligned} \quad (5)$$

where ϵ is the ellipticity, δ measures the deviation from axisymmetry, and θ is the wobble angle between \hat{e}_3 and \mathbf{L} .

Before investigating the dynamics of free precession, we first give an estimation of ϵ . The shear stresses of the crystallized solid crust can prevent a small fraction of the hydrostatic rotational bulge from aligning with the instantaneous spin axis. We denote the ellipticity sourced from elastic deformation as ϵ_c . The upper limit of ϵ_c is approximated as (Ushomirsky et al. 2000; Haskell et al. 2006; Johnson-McDaniel & Owen 2013; Gittins et al. 2020; Morales & Horowitz 2022)

$$\epsilon_c^{\text{max}} \approx 10^{-6} \left(\frac{\sigma_{\text{br}}}{10^{-1}} \right), \quad (6)$$

where the breaking strain $\sigma_{br} \sim 0.1$ is taken from the molecular dynamics simulations of crustal fracture in Horowitz & Kadau (2009). The actual value of ϵ_c depends on the evolution history of the star and is hard to estimate. It may be much smaller than ϵ_c^{\max} since plastic processes may relieve the strain in long time evolution.

The magnetic fields inside the star create deformation because non-radial field gradients can support non-radial matter-density gradients in hydromagnetic equilibrium. However, the strength and geometry of the internal magnetic fields are still very uncertain. The magnetic ellipticity ϵ_B is on the order of the magnetic energy over the gravitational energy

$$\epsilon_B = \frac{\kappa H \bar{B} R^4}{M^2} \approx 1.93 \times 10^{-6} \kappa R_6^4 M_{1.4}^{-2} H_{15} \bar{B}_{15}, \quad (7)$$

which is a crude estimation but consistent with more rigorous calculations (see e.g., Haskell et al. 2008; Akgun & Wasserman 2008; Lander & Jones 2009; Ciolfi et al. 2010; Mastrano et al. 2013). Here \bar{B} is the volume average of the internal magnetic field, \bar{B}_{15} represents the magnetic field in units of 10^{15} G, $H = \bar{B}$ for a normal conducting interior while $H \approx 10^{15}$ G if the core sustains protons in the type II superconducting state (Wasserman 2003; Cutler et al. 2003). The parameter κ can be positive or negative depending on the relative strength between the poloidal and toroidal components of the internal magnetic field. One can quickly notice that, magnetars with large internal magnetic fields may cause large magnetic deformation.

Most earlier studies have been devoted to axisymmetric magnetic field, regardless of whether the magnetic field is poloidal, toroidal or “mixed”. The star is deformed into a biaxial shape with the deformation axis along the dipole field. We relax this axisymmetric assumption and study a more general case with triaxial deformations and misalignment between the magnetic dipole and deformation axes. On the one hand, the tilted poloidal-toroidal configuration is more general and not physically forbidden (Lasky & Melatos 2013; Wasserman et al. 2022). For instance, Lasky & Melatos (2013) obtained a tilted torus magnetic field from magnetohydrodynamic (MHD) simulation, which is stable but the equilibrium state could not be specified freely (Glampedakis & Lasky 2016). On the other hand, multipolar magnetic fields may exist in the interior of magnetars. Mastrano et al. (2013, 2015) found that the mixed odd and even multipoles can create a deformation that is misaligned with the magnetic dipole axis even if the magnetic field is axisymmetric. Moreover, the mixture of elastic and magnetic deformations can produce a triaxial shape (Wasserman 2003; Glampedakis & Jones 2010).

The relative strength between the poloidal and toroidal fields is also not clear. There is no stable mixed poloidal-toroidal field in NSs for a barotropic normal fluid (Lander & Jones 2012). According to MHD simulations, Braithwaite (2009) argued that an axisymmetric field is stable in stratified fluid if the poloidal field is much weaker than the toroidal field. In this case, the deformation is prolate. Lander (2013) presented the first self-consistent superconducting NS equilibria with poloidal and mixed poloidal-toroidal fields. The poloidal component was dominant in all the configurations that Lander (2013) studied.

According to the above discussions on the deformations and the structures of the internal magnetic fields, we give following arguments and assumptions.

- (i) Generally, the deformed NS is in a triaxial shape. The biaxial case is only a good approximation if the deformation is along a specific axis.
- (ii) The external magnetic axis is not necessarily aligned with any deformation axes.
- (iii) The ellipticity can be positive or negative depending on the magnetic field geometry and possible elastic deformations.

(iv) The precession of magnetically distorted NSs differs qualitatively from the elastic body precession although they have the same mathematical form. There are slow and non-rigid internal motions in addition to the uniform rotation (Mestel & Takhar 1972; Lander & Jones 2017). Although these non-rigid motions are important for the evolution of the magnetic inclination angle, we ignore them in this work since they are higher-order effects.

3 DYNAMICS OF PRECESSION

3.1 Free precession

The Euler equation of a freely-precessing body is (Landau & Lifshitz 1960)

$$\dot{\mathbf{L}} + \boldsymbol{\omega} \times \mathbf{L} = 0, \quad (8)$$

where the dot denotes the derivative with respect to time t . Eq. (8) can be solved analytically in terms of Jacobian elliptic functions (Landau & Lifshitz 1960; Wasserman 2003; Akgun et al. 2006; Gao et al. 2020; Wasserman et al. 2022). The angular momentum \mathbf{L} and the kinetic energy E are conserved for free precession. Different branches of the solutions are determined by the relation between L^2 and $2EI_2$. One usually sets $\omega_2 = 0$ at the initial time $t = 0$. Thus, the solutions are also equivalently determined by the parameter

$$m = \delta \tan^2 \theta_0, \quad (9)$$

with θ_0 denoting the wobble angle θ at $t = 0$.

When $m < 1$ ($L^2 > 2EI_2$), the precession is around \hat{e}_3 and the components of the unit angular momentum $\hat{\mathbf{L}} \equiv \mathbf{L}/L$ are

$$\begin{aligned} \hat{L}_1 &= \sin \theta_0 \operatorname{cn}(\omega_p t, m), \\ \hat{L}_2 &= \sin \theta_0 \sqrt{1 + \delta} \operatorname{sn}(\omega_p t, m), \\ \hat{L}_3 &= \cos \theta_0 \operatorname{dn}(\omega_p t, m), \end{aligned} \quad (10)$$

where cn , sn , and dn are Jacobi elliptic functions (see Appendix A for more details), and

$$\omega_p = \frac{\epsilon L \cos \theta_0}{I_3 \sqrt{1 + \delta}}. \quad (11)$$

The time evolution of the angular frequencies in the body frame is periodic with a period

$$T = \frac{4I_3}{\epsilon L \cos \theta_0} \sqrt{1 + \delta} K(m), \quad (12)$$

where $K(m)$ is the complete elliptic integral of the first kind. One can notice that $2\pi/\omega_p$ is not equal to the period T because the Jacobi elliptic functions are not periodic in 2π , but rather periodic in $4K(m)$. In Fig. 1, we illustrate the geometry and the motion in the corotating body frame. The angular momentum precesses around \hat{e}_3 with a period T . Following the definition in Cutler & Jones (2001), we call T the free precession period of the deformed NS. The wobble angle θ nutates with a period $T/2$.

When $m = 1$, the solution is unstable and the trajectories of the angular momentum will decay exponentially to the intermediate axis \hat{e}_2 . The detailed solution can be found in Landau & Lifshitz (1960). We omit this special case.

When $m > 1$, the precession is around \hat{e}_1 and the solutions are given in Akgun et al. (2006) and Zanazzi & Lai (2015). We want to retain the definition of θ as the angle between $\hat{\mathbf{L}}$ and \hat{e}_3 , which is helpful to map the latter calculations to the $m < 1$ case directly. So,

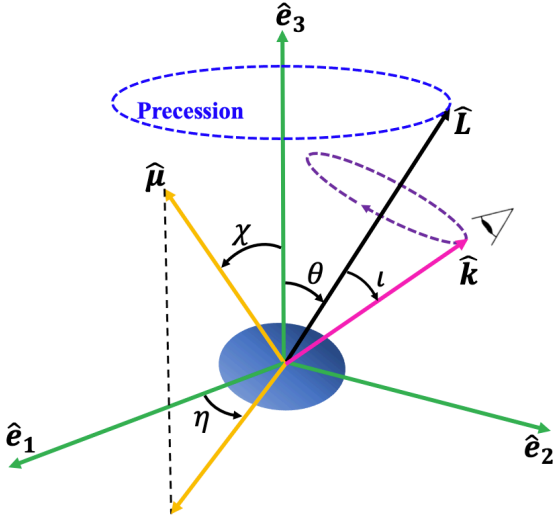


Figure 1. The geometry and the motion of a deformed NS in the corotating body frame. The NS precesses around \hat{e}_3 with period T , which is called the *free precession period* of the NS. The wobble angle θ between \hat{e}_3 and \hat{L} nutates with a period of $T/2$. For the special biaxial case, the wobble angle θ is fixed. An observer views the NS in a direction \hat{k} fixed in the inertia frame but rotating around \hat{L} in the body frame with spin angular frequency ω with an inclination angle ι . The direction of the dipole moment $\hat{\mu}$ is fixed in the body frame and is described by the polar angle χ and the azimuthal angle η .

we make a redefinition of the basis vectors,

$$\begin{aligned}\hat{e}_1 &= \hat{e}_3, \\ \hat{e}_2 &= -\hat{e}_2, \\ \hat{e}_3 &= \hat{e}_1.\end{aligned}\quad (13)$$

Then the solutions of \hat{L} can be represented in an identical form to the $m < 1$ case, except for $I_1 \geq I_2 \geq I_3$. Note that $\epsilon < 0$ and the precession direction is opposite to the $m < 1$ case.

A biaxial body corresponds to the special cases of oblate deformation ($\delta = 0, \epsilon > 0$) or prolate deformation ($\delta = 0, \epsilon < 0$). Eq. (10) degenerates into the form

$$\begin{aligned}\hat{L}_1 &= \sin \theta_0 \cos(\omega_p t), \\ \hat{L}_2 &= \sin \theta_0 \sin(\omega_p t), \\ \hat{L}_3 &= \cos \theta_0,\end{aligned}\quad (14)$$

where

$$\omega_p = \epsilon L \cos \theta_0 / I_3, \quad (15)$$

becomes the precession frequency, and the precession period is

$$T = \frac{2\pi}{|\omega_p|} = \frac{2\pi I_3}{|\epsilon| L \cos \theta_0}. \quad (16)$$

In later examples, we only study the $m < 1$ branch, the cases for $m > 1$ can be easily obtained by redefining $I_1 \geq I_2 \geq I_3$. Although the precession period T is different for distinct NS geometries, we can roughly estimate the timescale of the precession as

$$\tau_p = \frac{P}{\epsilon} = 1.58 P_5 \epsilon_7^{-1} \text{ yr}, \quad (17)$$

where $\epsilon_7 = \epsilon / 10^{-7}$. The angular velocity in the body frame is

$$\omega = L \left(\frac{\hat{L}_1}{I_1} + \frac{\hat{L}_2}{I_2} + \frac{\hat{L}_3}{I_3} \right) = \frac{L}{I_3} \left(\frac{I_3 \hat{L}_1}{I_1} + \frac{I_3 \hat{L}_2}{I_2} + \hat{L}_3 \right). \quad (18)$$

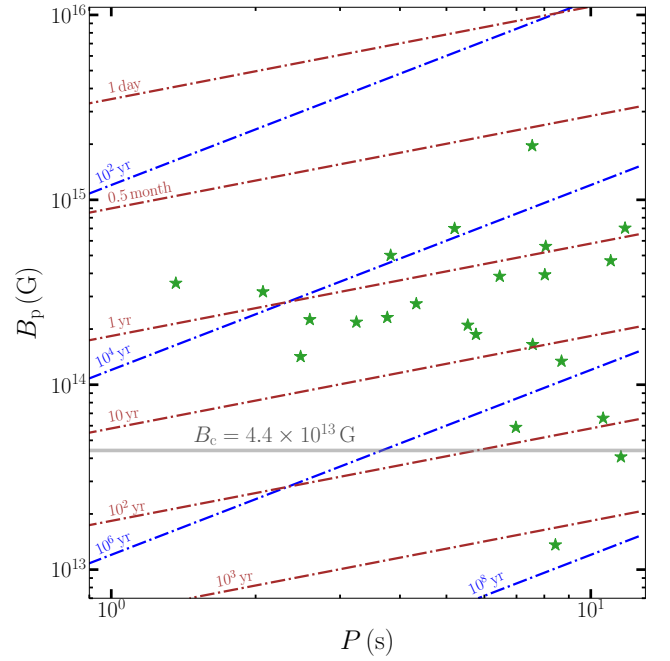


Figure 2. The relation between the spin period P and the magnetic field at the magnetic pole B_p for magnetars with measured period and period derivative (green). Lines of constant τ_{rad} (blue) and constant τ_m (brown) are also illustrated. The horizontal gray line represents the Schwinger limit of the magnetic field, $B_c = 4.4 \times 10^{13}$ G.

It is obvious that the angle θ' between the angular momentum L and the angular velocity ω is on the order of $\theta' \sim \epsilon \theta \ll 1$. We can approximate $L \parallel \omega$ to the zeroth order of ϵ when we evaluate the geometry of the NS. We denote the unit vector of the angular frequency as $\hat{\omega} \equiv \omega / \omega_0$, where ω_0 is the magnitude of the angular frequency at $t = 0$. For simplicity, we also take the external magnetic field as a dipole field. The dipole moment, $\mu = \mu \hat{\mu}$, is fixed in the body frame and

$$\hat{\mu} = \hat{\mu}_1 \hat{e}_1 + \hat{\mu}_2 \hat{e}_2 + \hat{\mu}_3 \hat{e}_3 = (\sin \chi \cos \eta, \sin \chi \sin \eta, \cos \chi). \quad (19)$$

Note that the angle η is not necessarily zero in the general triaxial case. Only in the biaxial case can one choose $\eta = 0$ due to the axisymmetry of the NS.

3.2 Forced precession

For magnetars, large magnetic fields also indicate large electromagnetic torques. Generally, rotating NSs endowed with external magnetic fields have two kinds of electromagnetic torques acting on it. The first one is the far-field torque (the so-called spin-down torque), which originates from the fact that the electromagnetic emission carries away angular momentum (Deutsch 1955; Davis & Goldstein 1970). For a dipole field, we express the far-field torque N_{rad} as

$$N_{\text{rad}} = \frac{k_1 \mu^2 \omega^3}{c^3} [(\hat{\omega} \cdot \hat{\mu}) \hat{\mu} - k_2 \hat{\omega}], \quad (20)$$

where k_1 and k_2 are numerical constants on the order of unity.

For the simplest vacuum dipole, $k_1 = 2/3$, $k_2 = 1$ (Deutsch 1955; Davis & Goldstein 1970), and the rotational energy dissipates at a rate

$$N_{\text{rad}} \cdot \omega = -\frac{2\mu^2 \omega^4 \sin^2 \alpha}{3c^3}, \quad (21)$$

where α is the magnetic inclination angle between $\hat{\omega}$ and $\hat{\mu}$. There is no dissipation for the vacuum dipole case when the angular velocity and the dipole moment are aligned, namely $\sin \alpha = 0$.

Although the vacuum magnetosphere torque predicts the spin-down rate somehow close to the observed values for pulsars, the magnetosphere is filled with plasma in reality. The charges and currents in the plasma inevitably modify the structure of magnetosphere. There are no analytical expressions for the far-field torque for a plasma-filled magnetosphere. Li et al. (2012) and Philippov et al. (2014) analyzed the results of force-free MHD simulations and found that the plasma-filled torque can be approximately parameterized by taking $k_1 \simeq 1$ and $k_2 \simeq 2$ if the weak dependence on R/R_{LC} is ignored, with R_{LC} being the radius of the light cylinder. This parametrization of the far-field torque was also applied to study the precession of pulsars (Arzamasskiy et al. 2015). In this case, the rotational energy dissipates at a rate

$$N_{\text{rad}} \cdot \omega = -\frac{\mu^2 \omega^4}{c^3} (1 + \sin^2 \alpha). \quad (22)$$

The energy still can be dissipated when $\alpha = 0$ compared to the vacuum case. The form of the plasma-filled torque is equivalent to adding a parallel component compared to the vacuum case.

The far-field torque not only dissipates the rotational energy but changes the geometry of the star, such as the wobble angle and the magnetic inclination angle. We define the spin-down timescale induced by the far-field torque as

$$\tau_{\text{rad}} = \frac{3c^3 I_0}{2\mu^2 \omega^2} = 3.61 \times 10^5 M_{1.4} P_5^2 B_{14}^{-2} \text{ yr}. \quad (23)$$

The second kind of the electromagnetic torque is the near-field torque, which arises from the inertia of the external magnetic field (Davis & Goldstein 1970; Good & Ng 1985; Melatos 1997). The near-field torque is denoted by N_{m} and can be expressed as

$$N_{\text{m}} = \frac{k_3 \omega^2 \mu^2}{Rc^2} (\hat{\omega} \cdot \hat{\mu}) (\hat{\omega} \times \hat{\mu}), \quad (24)$$

where the external magnetic field is assumed to be a dipole field. Using different methods, many authors have obtained slightly different values of k_3 (Goldreich 1970; Good & Ng 1985; Melatos 2000; Beskin et al. 2013; Zanazzi & Lai 2015). Here, we adopt the value $k_3 = 3/5$, which is consistent with Melatos (1997) and Zanazzi & Lai (2015). This value can be obtained by assuming a uniform internal magnetic field \mathbf{B}_{p} rotating rigidly around the spin axis, and the electric field given by $\mathbf{E} = -(\mathbf{v}/c) \times \mathbf{B}_{\text{p}}$ for a perfectly conducting fluid. Although an internal electromagnetic field is assumed, the near-field torque in Eq. (24) only depends on the exterior electromagnetic field of the NS (Beskin & Zheltoukhov 2014; Zanazzi & Lai 2015).

The near-field torque is perpendicular to ω and scales as ω^2 . It does not dissipate energy or angular momentum but affects the spin and the wobble angle of the precessing NS in a timescale of

$$\tau_{\text{m}} = \frac{5RI_0 c^2}{3\omega \mu^2} = 16.8 M_{1.4} R_6 P_5 B_{14}^{-2} \text{ yr}. \quad (25)$$

In Fig. 2, we plot the relation between the dipole magnetic field at the magnetic pole B_{p} and the rotation period P for magnetars with measured period and period derivative (Olausen & Kaspi 2014).¹ We also plot the contour lines for τ_{m} and τ_{rad} . For typical magnetars with $B_{\text{p}} \sim 10^{14}$ – 10^{15} G, τ_{m} is on the order of 0.1–10 yr and τ_{rad} is on the order of 10^3 – 10^5 yr. It is very interesting that τ_{m} and the

free precession timescale τ_{p} could be comparable in some cases, and if so the free precession solution will be affected substantially. Melatos (1997, 2000) studied this effect and gave detailed numerical solutions for different NS geometries. In our work, we adopt an analytical method developed by Glampedakis & Jones (2010) and Zanazzi & Lai (2015) to study the precession dynamics under the near-field torque. Since τ_{rad} is much larger than τ_{m} and τ_{p} , we use a perturbative method to study the forced precession under the far-field torque following Goldreich (1970), Link & Epstein (2001), Wasserman (2003), and Wasserman et al. (2022).

3.2.1 Near-field torque

Under the near-field torque, the Euler equation is

$$\dot{\mathbf{L}} + \omega \times \mathbf{L} = \frac{3\omega^2 \mu^2}{5Rc^2} (\hat{\omega} \cdot \hat{\mu}) (\hat{\omega} \times \hat{\mu}). \quad (26)$$

The near-field torque arises from the inertia of the electromagnetic field, which can actually be absorbed into the moment of inertia tensor \mathbf{I} of the star (Melatos 2000; Glampedakis & Jones 2010; Zanazzi & Lai 2015). Eq. (26) can be written as

$$\dot{\mathbf{L}} + \omega \times (\mathbf{L} + \omega \cdot \mathbf{M}) = 0, \quad (27)$$

by introducing the effective deformation tensor

$$\mathbf{M} = -I_0 \epsilon_{\text{m}} (\hat{\mu} \otimes \hat{\mu}), \quad (28)$$

Here, ϵ_{m} is the effective ellipticity induced by the external magnetic field and

$$\epsilon_{\text{m}} = \frac{3\mu^2}{5I_0 R c^2} = 1.5 \times 10^{-9} M_{1.4}^{-1} B_{14}^2 R_6^3. \quad (29)$$

Since ϵ_{m} is quite small, we can introduce an effective moment of inertia tensor $\mathbf{I}_{\text{eff}} = \mathbf{I} + \mathbf{M}$ and write the Euler equations as (Zanazzi & Lai 2015)

$$\dot{\mathbf{L}}_{\text{eff}} + \omega \times \mathbf{L}_{\text{eff}} = 0, \quad (30)$$

with the effective angular momentum $\mathbf{L}_{\text{eff}} = \mathbf{I}_{\text{eff}} \cdot \omega$. Thus, the forced precession under the near-field torque is transformed into free precession by introducing a new prolate deformation along the magnetic dipole axis with an ellipticity ϵ_{m} . In principle, one can solve the forced-precession problem in Eq. (26) numerically, but the transformation used here gives analytical solutions and more insight into this problem. Therefore, we give the analytical solutions of the free precession in the effective principal frame. In practice, one just needs to substitute all the quantities in Sec. 3.1 into corresponding effective ones.

In Sec. 3.1, we assumed $\omega_2 = 0$ at $t = 0$ for simplicity. The phase of the precession is just $\omega_{\text{p}} t$. For consistency, one must be cautious of the initial phase when calculating the effective problem. For a general triaxial star, the magnetic dipole moment does not necessarily lie in the \hat{e}_1 - \hat{e}_3 plane ($\eta \neq 0$). Thus, the effective deformation caused by the near-field torque makes $\omega_{\text{eff},2} \neq 0$ at the initial time. So, the precession phase of the solutions should be $\omega_{\text{p,eff}} t + \psi_0$, where

$$\omega_{\text{p,eff}} = \frac{\epsilon_{\text{eff}} L_{\text{eff}} \cos \theta_{0,\text{eff}}}{I_{3,\text{eff}} \sqrt{1 + \delta_{\text{eff}}}}, \quad (31)$$

and the initial phase

$$\psi_0 = -\arcsin \sqrt{\frac{L_{2,\text{eff}}^2}{L_{1,\text{eff}}^2 + L_{2,\text{eff}}^2}}. \quad (32)$$

Only in the triaxial case with $\eta = 0$ and the special biaxial case, one

¹ <http://www.physics.mcgill.ca/~pulsar/magnetar/main.html>

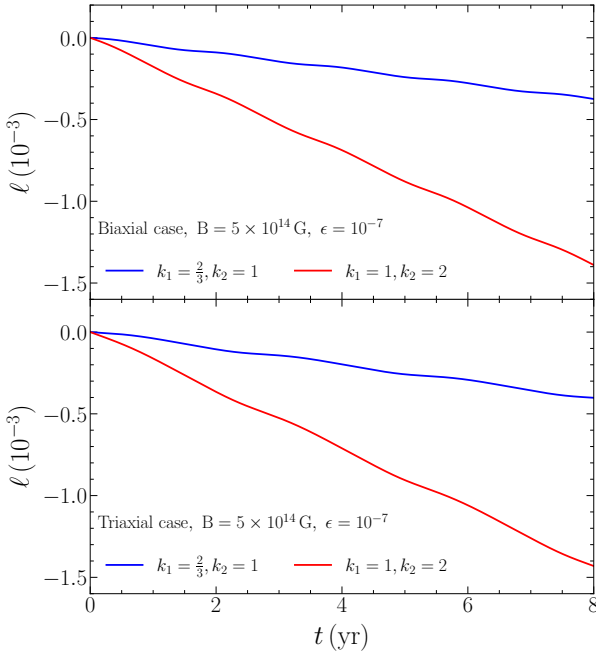


Figure 3. The fractional change of the angular frequency due to spin down for the biaxial case (upper) and the triaxial case (lower). For comparison, both of the vacuum torque ($k_1 = 2/3, k_2 = 1$) and the plasma-filled torque ($k_1 = 1, k_2 = 2$) are illustrated. The parameters for the biaxial and triaxial cases are shown in Case I and Case II of Table 1 respectively.

can take $\psi_0 = 0$. Here, we denote the basis vectors, the eigenvalues of the moment of inertia tensor, the components of the angular velocity, the related geometric parameters in the effective principal frame with a lower index “eff” based on the quantities in the original principal frame. Generally, we find that the effects of the near-field torque can be ignored only if $\epsilon_m \lesssim 0.1\epsilon$.

3.2.2 Far-field torque

After absorbing the near-field torque into the effective moment of inertia tensor, the Euler equation under the far-field torque can be written as

$$\dot{\mathbf{L}}_{\text{eff}} + \boldsymbol{\omega} \times \mathbf{L}_{\text{eff}} = \mathbf{N}_{\text{rad}} = \frac{k_1 \mu^2 \omega^3}{c^3} [(\hat{\boldsymbol{\omega}} \cdot \hat{\boldsymbol{\mu}}) \hat{\boldsymbol{\mu}} - k_2 \hat{\boldsymbol{\omega}}]. \quad (33)$$

For simplicity, we omit the “eff” notation in later equations and only give “effective” parameters in specific examples. The far-field torque can be decomposed into parallel and perpendicular components with respect to the angular momentum

$$\mathbf{N}_{\text{rad}}^{\parallel} = \frac{k_1 \mu^2 \omega^3}{c^3} [(\hat{\boldsymbol{\omega}} \cdot \hat{\boldsymbol{\mu}})(\hat{\mathbf{L}} \cdot \hat{\boldsymbol{\mu}}) - k_2 (\hat{\mathbf{L}} \cdot \hat{\boldsymbol{\omega}})] \hat{\mathbf{L}}, \quad (34)$$

$$\mathbf{N}_{\text{rad}}^{\perp} = \mathbf{N}_{\text{rad}} - \mathbf{N}_{\text{rad}}^{\parallel} = \mathbf{N}_{\text{rad}} - (\hat{\mathbf{L}} \cdot \hat{\mathbf{N}}) \hat{\mathbf{L}}. \quad (35)$$

Taking the dot product between Eq. (33) and $\hat{\mathbf{L}}$, we obtain

$$\dot{L} = \mathbf{N}_{\text{rad}}^{\parallel} \cdot \hat{\mathbf{L}} \simeq \frac{3k_1 I_0 \omega}{2\tau_{\text{rad}}} (\cos^2 \alpha - k_2), \quad (36)$$

where $\hat{\mathbf{L}}$ and $\hat{\boldsymbol{\omega}}$ have been approximated as the same direction on the right-hand side. Eq. (36) determines the magnitude of the angular momentum. The angle α oscillates during the precession, which produces variability in the spin-down rate. The perpendicular Euler

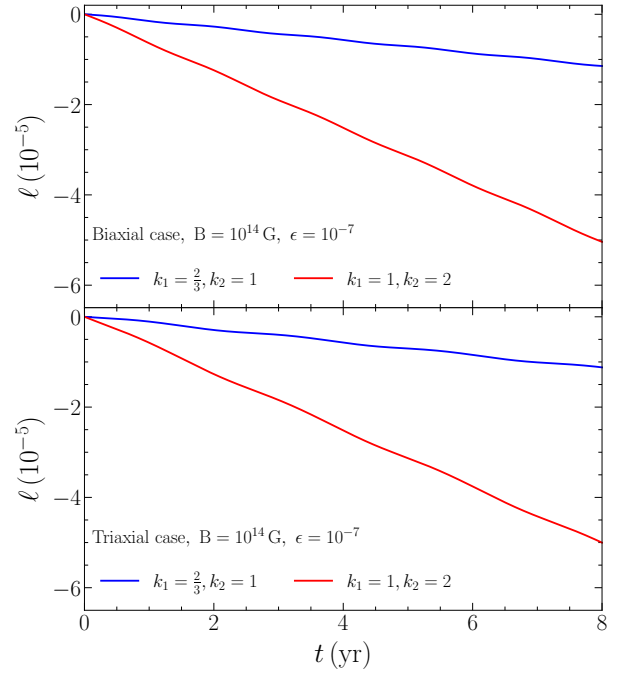


Figure 4. Same as Fig. 3 but for a deformed magnetar with $B = 10^{14}$ G. The parameters for the biaxial and triaxial cases are shown in Case III and Case IV of Table 1 respectively.

equation is

$$L \dot{\hat{\mathbf{L}}} + \boldsymbol{\omega} L (\hat{\boldsymbol{\omega}} \times \hat{\mathbf{L}}) = \mathbf{N}_{\text{rad}}^{\perp}, \quad (37)$$

which determines the direction of the angular momentum. The second term on the left-hand side arises from the precession of the angular momentum around $\hat{\boldsymbol{e}}_3$ in the body frame. The right-hand side is the term that originates from the far-field torque, which contributes to the secular change of θ and α .

In this work, we concentrate on the spin evolution on the precession timescale. According to Eq. (37), the angles θ and α change secularly on the order of $\sim \tau_p / \tau_{\text{rad}} \ll 1$ under the far-field torque. Thus, we can neglect the secular variation of α when calculating the change of the angular momentum with Eq. (36).

To describe the spin evolution, we introduce

$$\boldsymbol{\omega}(t) = \omega_0 (1 + \ell(t)), \quad (38)$$

where ω_0 is the angular frequency at the initial time $t = 0$, and ℓ is the fractional change of the angular frequency due to spin down. Since $\tau_p \ll \tau_{\text{rad}}$ and the spin-down rate is quite small, we can set $\omega = \omega_0$ on the right-hand side of Eq. (36) and write the solution of ℓ as

$$\ell = -\frac{3k_1}{2\tau_{\text{rad}}} \left(k_2 t - \int_0^t \cos^2 \alpha dt \right). \quad (39)$$

By introducing $\tau = \omega_p t + \psi_0$, the magnetic inclination angle α satisfies

$$\cos \alpha = \hat{\mu}_1 \sin \theta_0 \text{cn } \tau + \hat{\mu}_2 \sin \theta_0 (1 + \delta)^{1/2} \text{sn } \tau + \hat{\mu}_3 \cos \theta_0 \text{dn } \tau, \quad (40)$$

for the case of $m < 1$, where the modulus m has been omitted in the expressions of Jacobi elliptic functions. Substituting Eq. (A5) into Eq. (39), one gets the fractional change of the angular frequency for different NS geometries.

In Fig. 3, we show the fractional change of the angular frequency due to spin-down for both biaxial and triaxial cases with $B_p = 5 \times$

Table 1. The intrinsic and effective parameters for forced precession shown in Fig. 3-4.

| Case | Intrinsic parameters | | | | | | | Effective parameters | | | | | |
|------|----------------------|--------------------|------------|----------|----------------|------------|------------|-------------------------|-----------------------|-----------------------------|-------------------------|-------------------------|-----------------------|
| | P_0 (s) | B (G) | ϵ | δ | θ_0 (°) | χ (°) | η (°) | ϵ_{eff} | δ_{eff} | $\theta_{\text{eff},0}$ (°) | χ_{eff} (°) | η_{eff} (°) | T_{eff} (yr) |
| I | 5 | 5×10^{14} | 10^{-7} | 0 | 10 | 45 | 0 | 1.07×10^{-7} | 0.261 | 20.3 | 55.3 | 0 | 1.79 |
| II | 5 | 5×10^{14} | 10^{-7} | 1 | 10 | 45 | 45 | 9.99×10^{-8} | 1.15 | 20.5 | 60.2 | 36.1 | 2.59 |
| III | 5 | 10^{14} | 10^{-7} | 0 | 10 | 45 | 0 | 1.00×10^{-7} | 0.007 | 10.4 | 45.4 | 0 | 1.62 |
| IV | 5 | 10^{14} | 10^{-7} | 1 | 10 | 45 | 45 | 9.96×10^{-8} | 1.01 | 10.3 | 45.6 | 45.6 | 2.31 |

10^{14} G and $\epsilon = 10^{-7}$. The spin-down rate oscillates since α varies with the precession. The ellipticity induced by the near-field torque is $\epsilon_{\text{m}} = 3.75 \times 10^{-8} = 0.375\epsilon$. Thus, the near-field torque affects the precession substantially. The initial wobble angle for the motion is amplified from 10° to about 20° , which leads to large variations of the spin-down rate. We also plot the spin-down for both of the vacuum torque and the plasma-filled torque. The angular velocity decreases faster for the plasma-filled torque because the radiation power is stronger. From Eq. (39), we also notice that the second term on the right-hand side only depends on the coefficient k_1 .

We also give the case with $B_p = 10^{14}$ G and $\epsilon = 10^{-7}$ in Fig. 4. The ellipticity induced by the near-field torque is $\epsilon_{\text{m}} = 1.5 \times 10^{-9} = 0.015\epsilon$, which is negligible. The effective wobble angle is nearly the same as the free precession case and the variation of the spin-down rate is much smaller compared to the cases in Fig. 3. If $\epsilon \gtrsim 10^{-6}$ for the case with $B_p = 5 \times 10^{14}$ G, the effects of the near-field torque can be also neglected.

For the biaxial case with $\epsilon_{\text{m}} \ll \epsilon$ or the effective biaxial case, the parameters δ and η can be set to zero. The angle α satisfies

$$\cos \alpha = \sin \chi \sin \theta_0 \cos \omega_p t + \cos \chi \cos \theta_0, \quad (41)$$

and the integration of $\cos \alpha$ simplifies into

$$\int_0^t \cos^2 \alpha dt = \frac{1}{4\omega_p} \left[(\mu_1^2 + 2\mu_3^2) \omega_p t - (\mu_1^2 - 2\mu_3^2) \omega_p t \cos 2\theta_0 + 4\mu_1\mu_3 \sin 2\theta_0 \sin \omega_p t + \mu_1^2 \sin^2 \theta_0 \sin 2\omega_p t \right]. \quad (42)$$

where the initial phase $\psi_0 = 0$. The biaxial case in Fig. 4 can be obtained by taking Eq. (42) into Eq. (39) because $\epsilon_{\text{m}} \ll \epsilon$.

Our studies are similar to Melatos (1997), but we give analytical solutions and consider different models of the far-field torques. Compared to Akgun et al. (2006) and Wasserman et al. (2022), we have considered the effects of the near-field torque.

3.3 Precession dynamics in the inertial frame

The calculations in Secs. 3.1 to 3.2 are performed in the body frame of the NS. Before investigating the emissions from precessing magnetars, we give the geometry and the motion of the NS in the inertial frame, which is related to the body frame through a rotation matrix constructed from Euler angles ϕ , θ , and ψ (Landau & Lifshitz 1960). We take the basis of the inertial frame as \hat{e}_X , \hat{e}_Y , and \hat{e}_Z with \hat{L} parallel to \hat{e}_Z . The Euler angles satisfy

$$\begin{aligned} \cos \phi &= \hat{e}_X \cdot \hat{N}, \\ \cos \theta &= \hat{e}_3 \cdot \hat{e}_Z, \\ \cos \psi &= \hat{e}_1 \cdot \hat{N}, \end{aligned} \quad (43)$$

where $\hat{N} = \hat{e}_Z \times \hat{e}_3$. The time evolution of the Euler angles are given by

$$\begin{aligned} \cos \theta &= \hat{L}_3, \\ \tan \psi &= \hat{L}_1 / \hat{L}_2, \\ \dot{\phi} &= L / I_3 - \dot{\psi} / \hat{L}_3. \end{aligned} \quad (44)$$

Substituting the evolution of the angular momentum for different cases into Eqs. (44), one obtains the specific expressions for Euler angles. For the general triaxial case, the precession angle ψ and the wobble angle θ evolve with free precession period T , while the evolution of the angle ϕ is not periodic. Thus, the motion for a triaxial NS in the inertial frame is not periodic. We illustrate the geometry and the motion of the NS in the inertial frame in Fig. 5.

The components of $\hat{\mu}$ in the inertial frame are

$$\begin{aligned} \hat{\mu}_X &= \hat{\mu}_1 (\cos \psi \cos \phi - \cos \theta \sin \phi \sin \psi) \\ &\quad - \hat{\mu}_2 (\sin \psi \cos \phi + \cos \theta \sin \phi \cos \psi) + \hat{\mu}_3 \sin \theta \sin \phi, \\ \hat{\mu}_Y &= \hat{\mu}_1 (\cos \psi \sin \phi + \cos \theta \cos \phi \sin \psi) \\ &\quad + \hat{\mu}_2 (-\sin \psi \sin \phi + \cos \theta \cos \phi \cos \psi) - \hat{\mu}_3 \sin \theta \cos \phi, \\ \hat{\mu}_Z &= \hat{\mu}_1 \sin \theta \sin \psi + \hat{\mu}_2 \sin \theta \cos \psi + \hat{\mu}_3 \cos \theta, \end{aligned} \quad (45)$$

where $\hat{\mu}_1$, $\hat{\mu}_2$, and $\hat{\mu}_3$ are the components of $\hat{\mu}$ in the body frame in Eq. (19). The polar angle Θ and the azimuthal angle Φ of the magnetic dipole in the inertial frame satisfy

$$\begin{aligned} \Phi &= \arctan \left(\frac{\hat{\mu}_Y}{\hat{\mu}_X} \right), \\ \cos \Theta &= \hat{\mu}_Z. \end{aligned} \quad (46)$$

We can treat Θ as the magnetic inclination angle α because the angle between \hat{L} and $\hat{\omega}$ is first order in ϵ .

The time evolution of $\hat{\mu}$ is vital to determine the emission properties. The variations of the angle α during free precession lead to the swing of the emission regions and may modulate the beam shape parameters, polarization, and flux of the emission. While the precession also affects the rotational phase and time of arrivals of the emissions, which are closely related to the time evolution of Φ . In the following sections, we will first investigate the phase modulations and timing residuals buried in the time evolution of Φ , and then study the modulations of polarized radio/X-ray signals due to the variations of α during precession. Note that the calculations will be performed in the inertial frame.

4 TIMING RESIDUALS

In this section, we investigate the timing residuals of precessing magnetars, which may be used to search for precession from X-ray pulsations. The main manifestation of magnetars occurs in the X-ray energy band. Some magnetars are persistent X-ray sources with a luminosity $L_X \sim 10^{34} - 10^{35}$ erg s $^{-1}$ while others are transient

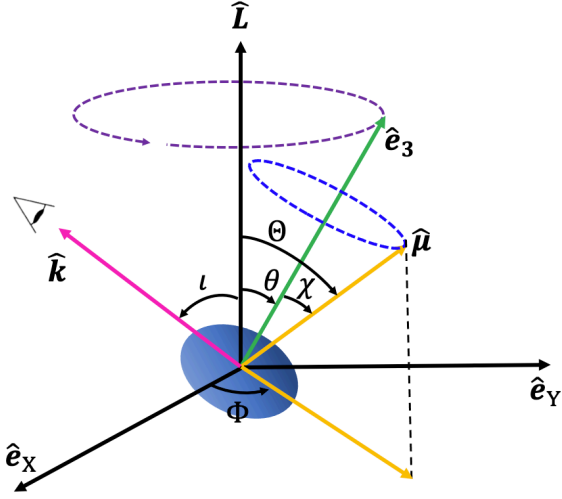


Figure 5. The geometry and the motion of a NS in the inertial frame. The NS rotates around $\hat{\mathbf{L}}$ with angular frequency ω . The NS itself rotates around $\hat{\mathbf{e}}_3$ with free precession period T , which is clockwise in the case of $m < 1$ and counterclockwise in the case of $m > 1$. The wobble angle θ between $\hat{\mathbf{e}}_3$ and $\hat{\mathbf{L}}$ nutates with period $T/2$. For the special biaxial case, the wobble angle θ is fixed. An observer in the $\hat{\mathbf{e}}_X$ - $\hat{\mathbf{e}}_Z$ plane views the NS in the direction $\hat{\mathbf{k}}$ with an inclination angle ι . The magnetic dipole $\hat{\boldsymbol{\mu}}$ is attached on the NS and is described by the polar angle Θ and azimuthal angle Φ .

that are much dimmer in quiescence, $L_X \lesssim 10^{32} \text{ erg s}^{-1}$ (Turolla et al. 2015; Makishima 2016; Kaspi & Beloborodov 2017). Most magnetars show clear X-ray pulsations due to the spin. The periods are clustered in the range $P = 2\text{--}12 \text{ s}$. Most of them show a large spin-down rate in the range of $\dot{P} = 10^{-13}\text{--}10^{-10} \text{ s s}^{-1}$. The timing of radio signals are also obtained for some transient magnetars.

The rotation phase and spin rate will be modulated since the emission direction rotates around $\hat{\mathbf{e}}_3$ during the precession. For simplicity, we assume that the emission is centered around the magnetic dipole axis $\hat{\boldsymbol{\mu}}$. As shown in Fig. 5, the observer sees the pulsation once the azimuthal angle of $\hat{\boldsymbol{\mu}}$ becomes

$$\Phi = 2\pi n, \quad (n = 0, 1, 2, \dots), \quad (47)$$

which is equivalent to $\mu_X > 0$ and $\mu_Y = 0$. Taking Eq. (45), the Euler angle ϕ at this epoch can be written as (Jones & Andersson 2001; Akgun et al. 2006)

$$\phi = 2\pi n + \frac{\pi}{2} + \arctan \phi_1, \quad (48)$$

where

$$\tan \phi_1 = \frac{\hat{\mu}_1 \cos \psi - \hat{\mu}_2 \sin \psi}{\hat{\mu}_2 \cos \theta \cos \psi - \hat{\mu}_3 \sin \theta + \hat{\mu}_1 \cos \theta \sin \psi}. \quad (49)$$

To obtain the timing residual, we first study the effective free precession case including the near-field torque. The Euler angle ϕ integrating from Eq. (44) is

$$\phi(t) = \phi_0 + \frac{L}{I_3} t + \frac{\sqrt{1 + \delta} \omega_p}{\cos \theta_0} \int_0^t \frac{dt}{1 + \delta \sin^2 \tau}, \quad (50)$$

where ϕ_0 is the initial phase of ϕ and $\tau = \omega_p t + \psi_0$. Combining Eq. (48) and Eq. (50), we obtain the time of arrival (TOA) t_n of the n -th pulse

$$\frac{L}{I_3} t_n = 2\pi n + \frac{\pi}{2} + \arctan \phi_1 - \phi_0 - \frac{\sqrt{1 + \delta} \omega_p}{\cos \theta_0} \int_0^{t_n} \frac{dt}{1 + \delta \sin^2 \tau}. \quad (51)$$

The TOA contains all the information of the precessing timing behaviours. To further investigate the spin modulations, we give the residuals of the period and the period derivatives. In practice, one first obtains the period $P_0 = 2\pi/\omega_0$ at some epoch t_0 , and finds the period derivative \dot{P}_0 that is attributed to the secular spin down. Then the period residuals can be determined by subtracting the two contributions

$$\Delta P = P(t) - P_0(t_0) - \dot{P}_0(t - t_0). \quad (52)$$

Since the precession timescale is much longer than the rotation timescale, we can approximate the differences by derivatives, and

$$\begin{aligned} \frac{L}{I_3} P - 2\pi &= \frac{L}{I_3} \Delta P_{\text{fp}} \\ &= \left(\frac{d \arctan \phi_1}{dt} - \frac{\sqrt{1 + \delta} \omega_p / \cos \theta_0}{1 + \delta \sin^2 \tau} \right) \frac{dt}{dn} \\ &= \left(\frac{d \arctan \phi_1}{dt} - \frac{\sqrt{1 + \delta} \omega_p / \cos \theta_0}{1 + \delta \sin^2 \tau} \right) P, \end{aligned} \quad (53)$$

where the period $P = t_n - t_{n-1}$, and ΔP_{fp} is the period residual owing to the free precession. By approximating $P \simeq P_0$ on the right-hand side, we get

$$\Delta P_{\text{fp}} = \left(\frac{d \arctan \phi_1}{d\tau} - \frac{\sqrt{1 + \delta} / \cos \theta_0}{1 + \delta \sin^2 \tau} \right) \frac{\epsilon \cos \theta_0 P_0}{\sqrt{1 + \delta}}. \quad (54)$$

For an effectively biaxial case or a biaxial case with $\epsilon_m \ll \epsilon$, we can set $\hat{\mu}_2 = 0$ and

$$\begin{aligned} \Delta P_{\text{fp}} &= -\epsilon \sin \theta_0 P_0 \\ &\times \left[\frac{\mu_1^2 \sin \theta_0 \sin^2 \omega_p t + \mu_3^2 \sin \theta_0 - \mu_1 \mu_3 \cos \theta_0 \cos \omega_p t}{(\mu_1 \cos \theta_0 \cos \omega_p t - \mu_3 \sin \theta_0)^2 + \mu_1^2 \sin^2 \omega_p t} \right], \end{aligned} \quad (55)$$

where the initial phase induced by the near-field torque $\psi_0 = 0$. Because ΔP_{fp} purely originates from the geometry of the free precession, we name ΔP as the geometric term of residual in period.

The far-field torque contributes to the period residual via the spin down

$$\frac{\Delta P_{\text{sd}}}{P} \simeq -\ell(t), \quad (56)$$

where $\ell(t)$ has been given in Eq. (39) with the integration of $\cos \alpha$ in Eq. (A5). For period residuals, we only care about the oscillation terms. After subtracting the secular terms, the period residual is

$$\begin{aligned} \Delta P_{\text{sd}} &= -\frac{3k_1 P_0}{2\tau_{\text{rad}}} \left(\int_0^t \cos^2 \alpha dt - \left\langle \int_0^t \cos^2 \alpha dt \right\rangle t \right) \\ &\simeq \frac{3k_1 P_0}{2\tau_{\text{rad}} \omega_p} \left\{ a_1 \text{cn } \tau + a_2 \text{sn } \tau + a_3 \text{dn } \tau \right. \\ &\quad \left. + a_4 \left[\frac{E(m)}{K(m)} \tau - E(\text{am } \tau) \right] + B_c \right\}, \end{aligned} \quad (57)$$

where $\langle \ell \rangle$ means an average over the precession period and

$$\begin{aligned} a_1 &= \sin 2\theta_0 (1 + \delta)^{\frac{1}{2}} \hat{\mu}_2 \hat{\mu}_3, \\ a_2 &= -\sin 2\theta_0 \hat{\mu}_1 \hat{\mu}_3 \text{sn}(\tau), \\ a_3 &= \frac{2 \cos^2 \theta_0 \hat{\mu}_1 \hat{\mu}_2 (1 + \delta)^{\frac{1}{2}}}{\delta}, \\ a_4 &= \frac{\cos^2 \theta_0}{\delta} \left[\hat{\mu}_1^2 - (1 + \delta) \hat{\mu}_2^2 + \hat{\mu}_3^2 \delta \right]. \end{aligned} \quad (58)$$

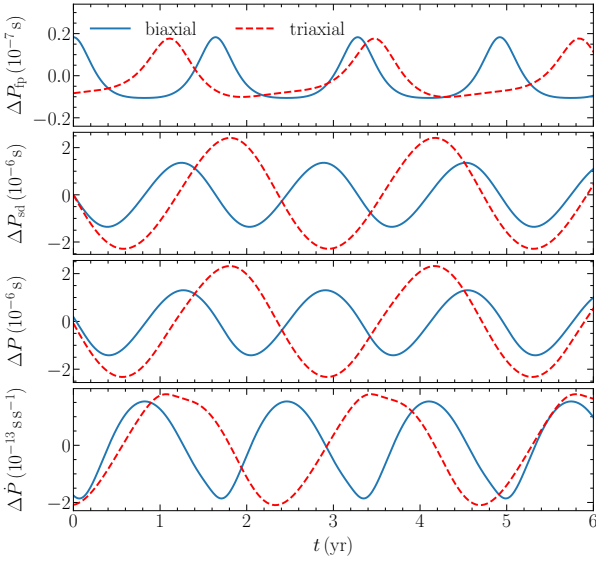


Figure 6. The residuals of the period and the period derivative for biaxial and triaxial NSs with $k_1 = 1$ and $k_2 = 2$. The parameters for the biaxial and triaxial cases are shown in Case I and Case II of Table 2 respectively. The initial period derivative is $\dot{P}_0 = 8.22 \times 10^{-13} \text{ s s}^{-1}$ for the biaxial case and $\dot{P}_0 = 8.82 \times 10^{-13} \text{ s s}^{-1}$ for the triaxial case.

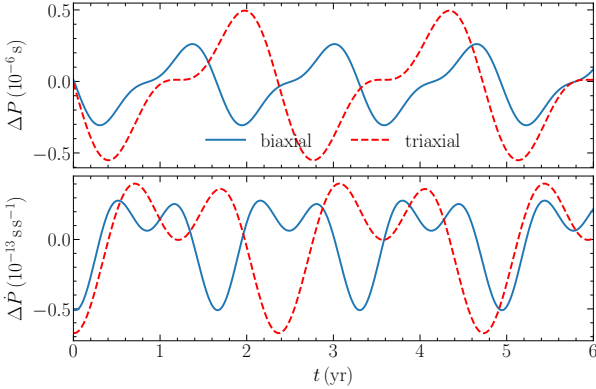


Figure 7. Same as Fig. 6, except for $\chi = 85^\circ$. The parameters for the biaxial and triaxial cases are shown in Case III and Case IV of Table 2 respectively. The initial period derivative is $\dot{P}_0 = 1.24 \times 10^{-12} \text{ s s}^{-1}$ for the biaxial case and $\dot{P}_0 = 1.27 \times 10^{-12} \text{ s s}^{-1}$ for the triaxial case.

The constant B_c is an integration constant, which can be easily obtained from $\Delta P_{\text{sd}}(t = 0) = 0$. For the special biaxial case, we set $\hat{\mu}_2 = 0$ and

$$\Delta P_{\text{sd}} = -\frac{3k_1 P_0}{2\tau_{\text{rad}}\omega_p} \times \left(\frac{1}{2} \sin 2\chi \sin 2\theta_0 \sin(\omega_p t) + \frac{1}{4} \sin^2 \theta_0 \sin^2 \chi \sin(2\omega_p t) \right), \quad (59)$$

which is consistent with Jones & Andersson (2001) and Link & Epstein (2001). We name the period residual resulting from the far-field torque as the spin-down term.

The total period residual ΔP can be expressed as

$$\Delta P = \Delta P_{\text{fp}} + \Delta P_{\text{sd}}. \quad (60)$$

Here the geometric term can be obtained from the effectively free

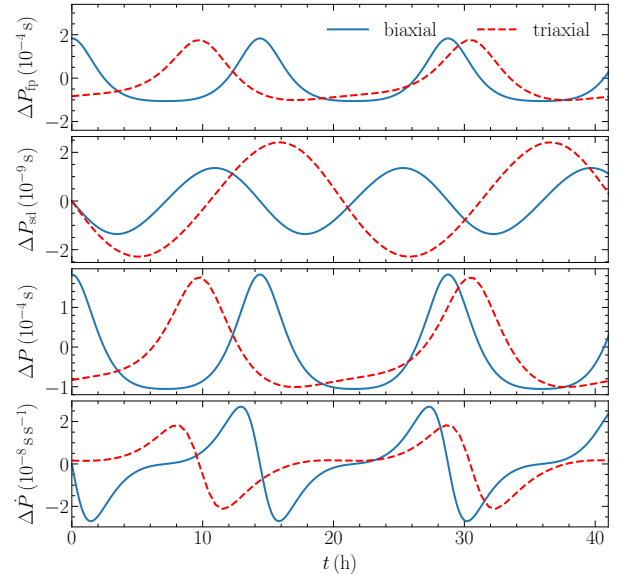


Figure 8. Same as Fig. 6, but with $\epsilon = 10^{-4}$. The parameters for the biaxial and triaxial cases are shown in Case V and Case VI of Table 2 respectively. The initial period derivative is $\dot{P}_0 = 8.22 \times 10^{-13} \text{ s s}^{-1}$ for the biaxial case and $\dot{P}_0 = 8.82 \times 10^{-13} \text{ s s}^{-1}$ for the triaxial case.

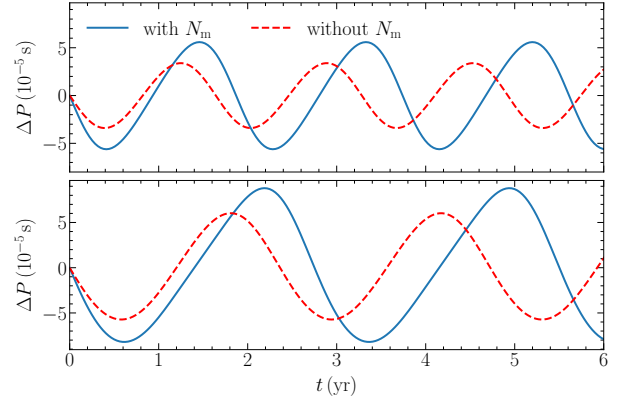


Figure 9. The period residual for a biaxial case (upper) and a triaxial case (lower) for $B = 5 \times 10^{14} \text{ G}$. The parameters for the biaxial and triaxial cases are shown in Case VII and Case VIII of Table 2 respectively. The period derivative $\dot{P}_0 = 2.06 \times 10^{-11} \text{ s s}^{-1}$ for the biaxial case and $\dot{P}_0 = 2.20 \times 10^{-11} \text{ s s}^{-1}$ for the triaxial case.

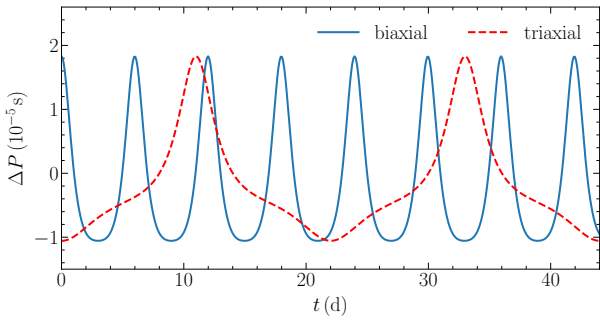
precession problem. While the spin-down term is determined by the far-field torque. The relative amplitude of the two terms depends on the geometry of the star. One notices that

$$\begin{aligned} \frac{\Delta P_{\text{fp}}}{P_0} &\sim \text{coefficient} \times \frac{P_0}{\tau_f}, \\ \frac{\Delta P_{\text{sd}}}{P_0} &\sim \text{coefficient} \times \frac{\tau_f}{\tau_{\text{rad}}}, \end{aligned} \quad (61)$$

where the coefficients are some geometric factors depending on the geometry of the deformed magnetars. When the free precession timescale τ_f is sufficiently long, corresponding to small ellipticities, the spin-down term dominates over the geometric term. This is the case for the possible precession of PSR B1828–11 (Link & Epstein 2001; Akgun et al. 2006). If the free precession timescale τ_f is closer to the spin period other than the spin-down timescale τ_{rad} ,

Table 2. The intrinsic and effective parameters for the timing residuals shown in Fig. 6–10.

| Case | Intrinsic parameters | | | | | | | Effective parameters | | | | | |
|------|----------------------|--------------------|------------|----------|-------------------------|---------------------|---------------------|-------------------------|-----------------------|--------------------------------------|----------------------------------|----------------------------------|-----------------------|
| | P_0 (s) | B (G) | ϵ | δ | θ_0 ($^\circ$) | χ ($^\circ$) | η ($^\circ$) | ϵ_{eff} | δ_{eff} | $\theta_{\text{eff},0}$ ($^\circ$) | χ_{eff} ($^\circ$) | η_{eff} ($^\circ$) | T_{eff} (yr) |
| I | 5 | 10^{14} | 10^{-7} | 0 | 15 | 45 | 0 | 1.00×10^{-7} | 7.61×10^{-3} | 15.4 | 45.4 | 0 | 1.65 |
| II | 5 | 10^{14} | 10^{-7} | 1 | 15 | 45 | 45 | 9.96×10^{-8} | 1.01 | 15.3 | 45.6 | 44.8 | 2.38 |
| III | 5 | 10^{14} | 10^{-7} | 0 | 15 | 85 | 0 | 1.01×10^{-7} | 0.0149 | 15.1 | 85.1 | 0 | 1.63 |
| IV | 5 | 10^{14} | 10^{-7} | 1 | 15 | 85 | 45 | 1.01×10^{-7} | 0.986 | 15.1 | 85.1 | 44.2 | 2.34 |
| V | 5 | 10^{14} | 10^{-4} | 0 | 15 | 45 | 0 | 1.00×10^{-4} | 7.50×10^{-6} | 15.0 | 45.0 | 0 | 0.00164 |
| VI | 5 | 10^{14} | 10^{-4} | 1 | 15 | 45 | 45 | 1.00×10^{-4} | 1.00 | 15.0 | 45.0 | 45.0 | 0.00236 |
| VII | 5 | 5×10^{14} | 10^{-7} | 0 | 15 | 45 | 0 | 1.07×10^{-7} | 0.261 | 25.3 | 55.3 | 0 | 1.87 |
| VIII | 5 | 5×10^{14} | 10^{-7} | 1 | 15 | 45 | 45 | 9.99×10^{-8} | 1.15 | 24.9 | 60.2 | 36.1 | 2.75 |
| IX | 5 | 10^{14} | 10^{-5} | 0 | 15 | 45 | 0 | 1.00×10^{-5} | 7.50×10^{-5} | 15.0 | 45.0 | 0 | 0.0164 |
| X | 5 | 10^{14} | 10^{-5} | 8 | 15 | 45 | 0 | 1.00×10^{-5} | 8.01 | 15.0 | 45.0 | 45.0 | 0.0603 |

**Figure 10.** The residuals of the period for biaxial and triaxial NSs. The parameters are shown in Case IX and Case X of Table 2 respectively. The initial period derivative is $\dot{P}_0 = 8.22 \times 10^{-13} \text{ s s}^{-1}$ for the biaxial case and $\dot{P}_0 = 8.82 \times 10^{-13} \text{ s s}^{-1}$ for the triaxial case.

corresponding to large ellipticities, the geometric term will dominate. This is the case for the possible precession of 4U 0142+61 (Makishima et al. 2014).

When $m > 1$, the ellipticity is negative. Thus the precession direction is opposite to the case of $m < 1$. If we change ϵ into $-\epsilon$ and keep the other parameters fixed, the geometric term changes sign while the spin-down term stays the same. The amplitude of the period residual due to vacuum torque is just 2/3 times that of the plasma-filled torque. In following examples, we only study the timing residuals of the case with $k_1 = 1$.

To study the effects of the NS geometries and the near-field torque separately, we first neglect the contributions of the near-field torque by taking $\epsilon = 10^{-7}$ and $B = 10^{14} \text{ G}$, where $\epsilon_m = 0.015\epsilon \ll \epsilon$. In Fig. 6, we give an example of $\Delta P_{\text{sd}} \gg \Delta P_{\text{fp}}$. The spin-down term dominates over the geometric term by a factor of ~ 10 . The morphologies for the biaxial case and the triaxial case are basically the same. The main differences are the amplitude and the period of the modulations.

Another important feature is that ΔP does not deviate much from a single harmonic. We take the biaxial case as an example to understand this point. The triaxial case can be understood in the same way qualitatively. For the biaxial case, the spin-down term ΔP_{sd} has components both at frequencies ω_p and $2\omega_p$. The amplitude of ΔP_{sd} at ω_p is larger than the harmonics at $2\omega_p$ only if $\cot \theta > \tan \chi/8$. For the biaxial case in Fig. 6, $\cot \theta = \cot \theta_0 = 3.73$ while $\tan \chi/8 = 0.125$.

The residuals at ω_p is about 30 times larger. Therefore, the residuals mainly come from the term at the frequency ω_p of the spin-down contribution.

For the biaxial case, the first harmonic at $2\omega_p$ of the spin-down term only plays an important role when $\cot \theta < \tan \chi/8$. So we present an example with $\chi = 85^\circ$ in Fig. 7 and keep other parameters fixed. One can notice that the residuals are quite different from that in Fig. 6 due to that the contribution at $2\omega_p$ is comparable with that at ω_p . While the geometric term is still about 0.1 of the spin-down term. The precession of PSR B1828–11 belongs to this kind.

To make the geometric term dominate over the spin-down term, the ellipticity should be sufficiently large. In Fig. 8, we show an example with $\epsilon = 10^{-4}$ and keep the other parameters the same as Fig. 6. The geometric term is much larger than the spin-down term by a factor $\sim 10^5$. The period residual is quite substantial and the effects of the electromagnetic torques are negligible.

Actually, such kind of modulations have been possibly observed by combined timing analysis of hard and soft X-rays for three magnetars, 4U 0142+61 (Makishima et al. 2014), 1E 1547.0–5408 (Makishima et al. 2021a), and SGR 1900+14 (Makishima et al. 2021b). Makishima et al. (2014, 2021a,b) gave the phase modulations of hard X-rays, which are physically equivalent to the timing residuals. In their model, the internal strong toroidal magnetic field creates a large prolate deformation along the magnetic dipole. The soft X-ray emission is centered around the magnetic dipole while the hard X-ray emission is somewhat misaligned with the magnetic dipole. This model is different from ours but can be simply obtained by redefining $\hat{\mu}$ as the emission direction of the hard X-rays in a direction other than the magnetic dipole and treating the star as a biaxial one. Thus, the period residual for 4U 0142+61 should be in the order of $\epsilon P \sim 0.001 \text{ s}$ according to Eq. (59). For the magnetar 4U 0142+61, Makishima et al. (2014) found that the rotation period at 8.69 s suffers slow phase modulations of 0.7 s, with a period of $\sim 15 \text{ h}$ in the hard X-ray band (15–40 keV), indicating an internal magnetic deformation $\epsilon \sim -1.6 \times 10^{-4}$ if the modulations are interpreted as free precession.

For the examples in Figs. 6–8, the near-field torque can be neglected. Thus, in Fig. 9, we show biaxial and triaxial examples with a large near-field torque. The amplitude of the residuals becomes larger compared to the cases without the near-field torque. The period of the modulations turns into T_{eff} .

In all above examples, the parameter m is on the order of 0.1. Although the period and amplitude of the residuals for the triaxial

cases are different from the biaxial ones, the morphologies are basically the same. It is easier to tell whether a NS is triaxial or not from the timing residuals if the parameter m is much larger. In Fig. 10, we show a triaxial example with $\delta = 8$, $\theta_0 = 15^\circ$, and $m = 0.574$. Since the wobble angle nutates in a wider range and the Jacobi elliptic functions deviate from the harmonic functions substantially, the morphology and period of the timing residuals for the triaxial case are quite different from the biaxial one.

5 MODULATIONS ON POLARIZATIONS

The Stokes parameters for the polarizations directly reflect the magnetic field rotating around the NS and the emission geometry. The precession leads to the swing of the emission and changes the polarization. In this section, we model the polarization of precessing magnetars and study the prospects of detecting the free precession with polarized X-ray and radio emissions.

5.1 Emission model of X-rays

We use the model developed by Ho & Lai (2003), Lai & Ho (2003), and van Adelsberg & Lai (2006) to calculate the soft thermal X-ray emission from the surface of a NS. We assume that the emission comes from a hot region, which is centered around the magnetic dipole axis, much smaller than the surface area of the star, and composed of a fully ionized hydrogen atmosphere with an effective temperature $T_{\text{eff}} \simeq 5 \times 10^6$ K. The magnetic field is also assumed to be a dipole field, which is approximately constant and normal to the stellar surface across the emission region.

In the highly magnetized plasma that characterizes the magnetosphere of NSs, X-ray photons propagate in the extraordinary mode (X mode) and the ordinary mode (O mode). The X mode is mostly polarized perpendicular to the \mathbf{k}_0 - \mathbf{B} plane while the ordinary mode (O mode) is mostly polarized within the \mathbf{k}_0 - \mathbf{B} plane, where \mathbf{k}_0 is the direction of photon propagation direction at the emission point and \mathbf{B} is the external magnetic field. The opacities for each mode are associated with the energy and the propagation direction of the X-ray photons, as well as the strength and the direction of the magnetic field in the magnetized plasma. The typical X mode opacity κ_X is much smaller than the O mode opacity κ_O (Meszaros 1992), satisfying $\kappa_X \sim (E/E_{Be})^2 \kappa_O$, where $E_{Be} = \hbar e B / m_e c$ is the electron cyclotron energy in the magnetic field. The decoupling density of the X mode photon ρ_X is much larger than that of the O mode photon ρ_O . As a result, the X mode photons can escape from deeper and hotter layers than the O mode photons. The emergent radiation is linearly polarized to a high degree (Gnedin & Sunyaev 1974; Meszaros et al. 1988; Pavlov & Zavlin 2000; Ho & Lai 2003; Lai & Ho 2003).

In strong magnetic fields, it has long been predicted that the vacuum becomes birefringent, and the dielectric tensor describing the atmospheric plasma of magnetars must be corrected for quantum electrodynamics (QED) vacuum effects (Heisenberg & Euler 1936; Tsai & Erber 1975). At the vacuum resonance, the contributions of the plasma and the vacuum to the dielectric tensor cancel each other (Lai & Ho 2003). When a photon with energy E traverses through the density gradient of the plasma, it will encounter the vacuum resonance at the density

$$\rho_V = 0.96 Y_e^{-1} E_1^2 B_{14}^2 f_B^{-2} \text{ g cm}^{-3}, \quad (62)$$

where $Y_e = Z/A$ with Z and A the charge number and mass number of the ion respectively, $E_1 = E/(1 \text{ keV})$, and f_B is a slowly varying function of B that is on the order of unity. If the density variations of

the plasma are sufficiently gentle as the photon propagates through the inhomogeneous plasma, an X mode (O mode) photon will be converted into an O mode (X mode) photon when it traverses the vacuum resonance. For the mode conversion to be effective, the adiabatic condition $E \geq E_{\text{ad}}$ must be satisfied (Ho & Lai 2003; Lai & Ho 2003), with

$$E_{\text{ad}} = 2.52 \left[f_B \tan \theta_{\text{KB}} \left| 1 - (E_{\text{Bi}}/E)^2 \right| \right]^{2/3} \left(\frac{1 \text{ cm}}{H_\rho} \right)^{1/3}. \quad (63)$$

Here θ_{KB} is the angle between the magnetic field and the photon propagation direction, E_{Bi} is the ion cyclotron energy, and H_ρ is the density scale-height along the ray. For a photon with energy $E \sim E_{\text{ad}}$, it undergoes partial mode conversion. In general, the mode conversion probability of a photon is (Lai & Ho 2003)

$$P_c = 1 - \exp \left[-(\pi/2) (E/E_{\text{ad}})^3 \right]. \quad (64)$$

To obtain the emergent intensities, one needs to solve the radiative transfer equations (RTEs) of the two modes subject to the constraints of hydrostatic and radiative equilibria (Ho & Lai 2001, 2003). van Adelsberg & Lai (2006) provided the fitting formulae of the temperature profile for different atmospheric models with different magnetic fields B and effective temperatures T_{eff} . Once the temperature profile is known, the emergent intensities can be obtained by a single integration of the RTEs. We use the fitted temperature profile and integrate the RTEs including the vacuum effect following van Adelsberg & Lai (2006). The spectral intensities for the X mode photons $I_X(\theta_{\text{em}})$ and the O mode photons $I_O(\theta_{\text{em}})$ at different emission angles θ_{em} are obtained. The ‘‘intrinsic’’ linear polarization fraction at the emission point is defined as

$$\Pi_{\text{em}} = \frac{I_O(\theta_{\text{em}}) - I_X(\theta_{\text{em}})}{I_O(\theta_{\text{em}}) + I_X(\theta_{\text{em}})}, \quad (65)$$

where θ_{em} is the angle between the photon propagation direction and the surface normal.

To determine the polarization state of the signals, one must consider the propagation of polarized radiation in the magnetosphere of magnetars, whose dielectric properties are dominated by the vacuum polarization in the X-ray band (Heyl et al. 2003). When an X-ray photon propagates in the magnetosphere, its polarization state evolves adiabatically along the varying magnetic field up to the polarization limiting radius r_{pl} , which is far from the surface of the NS. Thus, the observed Stokes parameters are determined by the ‘‘frozen’’ polarization state at r_{pl} . Adiabatic evolution of the photon modes in the magnetosphere leads to a significant polarization fraction even when the emission comes from extended regions on the surface (Heyl et al. 2003; Fernandez & Davis 2011; Taverna et al. 2015). In contrast, if the polarization state is determined by the emission at the surface, additions of the Stokes parameters from distinct regions tend to cancel each other and lead to low polarization fraction.

The magnetic field direction that determines the polarization can be characterized by the polar angle Θ and the azimuthal angle Ψ . As shown in Fig. 11, the polar angle between the magnetic dipole field and the line of sight satisfies

$$\cos \Theta = \cos \iota \cos \alpha + \sin \iota \sin \alpha \cos \Phi. \quad (66)$$

The azimuthal angle Ψ is the position angle (PA) of the polarized emission. To obtain the PA, we project the dipole field onto the $\hat{\mathbf{i}}$ - $\hat{\mathbf{j}}$ plane. Introducing the polarization basis

$$\begin{aligned} \hat{\mathbf{e}}_1^{\text{p}} &= \frac{(\hat{\mathbf{k}} \times \hat{\boldsymbol{\mu}}) \times \hat{\mathbf{k}}}{\sin \Theta}, \\ \hat{\mathbf{e}}_2^{\text{p}} &= \frac{\hat{\mathbf{k}} \times \hat{\boldsymbol{\mu}}}{\sin \Theta}, \end{aligned} \quad (67)$$

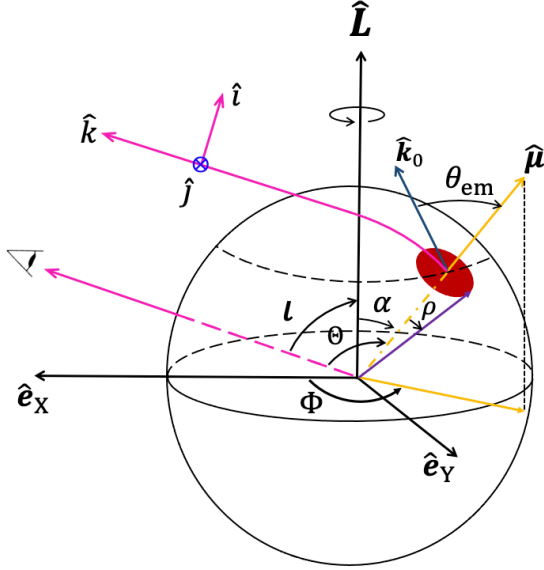


Figure 11. The X-ray emission geometry. The observer lies in the \hat{e}_X - \hat{e}_Z plane at an inclination angle ι . A hotspot is located at one of the magnetic poles. An X-ray photon emitted at an angle θ_{em} respect to the surface normal will be received at colatitude Θ due to the light bending effect. A coordinate system IJK with the basis $\{\hat{i}, \hat{j}, \hat{k}\}$ is introduced, where \hat{k} is along the line of sight, \hat{i} lies in the plane spanned by the line of sight and the angular momentum \hat{L} , and \hat{j} is determined by $\hat{L} \times \hat{k} = -\hat{j} \sin \iota$.

the PA measured from the projection of the spin axis onto the plane of the sky in the counterclockwise direction is given by

$$\cos \Psi = \hat{e}_1^p \cdot \hat{i} = \frac{\sin \iota \cos \alpha - \cos \iota \sin \alpha \cos \Phi}{\sin \Theta}, \quad (68)$$

$$\sin \Psi = \hat{e}_1^p \cdot \hat{j} = -\frac{\sin \alpha \sin \Phi}{\sin \Theta}. \quad (69)$$

Then, we obtain the expressions of PA in the RVM as (Radhakrishnan & Cooke 1969; Lorimer & Kramer 2005)

$$\tan \Psi = \frac{\sin \alpha \sin \Phi}{\cos \iota \sin \alpha \cos \Phi - \sin \iota \cos \alpha}. \quad (70)$$

The rotation phase at the polarization limiting radius is $\Phi(r_{\text{pl}}) = \Phi(R) + r_{\text{pl}}/R_{\text{LC}}$, where $\Phi(R)$ is the rotation phase when the photon is emitted at the surface. Magnetars rotate slowly, with $r_{\text{pl}}/R_{\text{LC}} \ll 1$ and $\Phi(r_{\text{pl}}) \approx \Phi(R)$.

In principle, one needs to evolve the polarization state along the magnetic field to determine Ψ for different points on the extended hotspot (Heyl et al. 2003; Taverna et al. 2015). However, we consider a hot region much smaller than the surface area of magnetars and the magnetic field is constant across the emission region. Under this condition, the observed PA can be approximated as $\Psi(r_{\text{pl}}) \approx \pi + \Psi(R)$ (Lai & Ho 2003; van Adelsberg & Lai 2006). Therefore, the polarization state only changes with a constant phase shift compared to the intrinsic one. The Stokes parameters Q and U that are normalized to the total intensity I are

$$Q/I = \Pi_{\text{em}} \cos 2\Psi(r_{\text{pl}}), \quad (71)$$

$$U/I = \Pi_{\text{em}} \sin 2\Psi(r_{\text{pl}}). \quad (72)$$

To obtain the spectral ‘‘flux’’ of the Stokes parameters, the propagation effects in the curved spacetime such as the light bending and gravitational redshift need to be considered. In the IJK frame shown in Fig. 11, the points on the surface of the NS are described

by the azimuthal angle ϕ_h and polar angle θ_h . A photon emitted at an angle θ_{em} with respect to the surface normal escapes to infinity at a different angle θ_h due to the light bending effect in the curved spacetime. The relation between the two angles is given by the ray tracing function (Pechenick et al. 1983; Page 1995)

$$\theta_h(\theta_{\text{em}}) = \int_0^{R_s/2R} x \left[\left(1 - \frac{R_s}{R}\right) \left(\frac{R_s}{2R}\right)^2 - (1-2u)u^2x^2 \right]^{-1/2} du, \quad (73)$$

where $x \equiv \sin \theta_{\text{em}}$, $R_s \equiv 2GM/c^2$ is the Schwarzschild radius. In a flat spacetime, the visible condition is simply $\cos \theta_h > 0$. The strong gravity of the NS allows the observer to see the region with negative $\cos \theta_h$. The critical value of $\cos \theta_h$ that defines the dark side of star is determined by the condition $\theta_{\text{em}} = 90^\circ$.

The differential spectral flux from the hotspot is (Pechenick et al. 1983; Beloborodov 2002)

$$\begin{aligned} dF_j(E_\infty, \Phi) &= \left(1 - \frac{r_g}{R}\right)^{1/2} I_j(\theta_{\text{em}}, E) \cos \theta_{\text{em}} \frac{d \cos \theta_{\text{em}}}{d \cos \theta_h} \frac{dS}{D^2} \\ &= \frac{R^2}{D^2} \left(1 - \frac{r_g}{R}\right)^{1/2} I_j(\theta_{\text{em}}, E) \sin \theta_{\text{em}} d \sin \theta_{\text{em}} d\phi_h \\ &= \frac{R^2}{D^2} \left(1 - \frac{r_g}{R}\right)^{1/2} I_j(\arcsin x, E) x dx d\phi_h, \end{aligned} \quad (74)$$

where $dS = R^2 \sin \theta_h d\theta_h d\phi_h$ is the visible surface element, D is the distance between the NS and the observer, I_j ($j = X, O$) are the specific intensities of the X and O mode photons at the emission point, and $E_\infty = (1 - R_s/R)^{1/2} E$ is the observed energy of the X-ray photons. The spectral flux then can be integrated as (Page 1995)

$$F_j(E_\infty, \Phi) = \frac{R^2}{D^2} \left(1 - \frac{r_g}{R}\right)^{1/2} \int_0^1 x I_j(\arcsin x, E) dx \int_0^{2\pi} d\phi_h. \quad (75)$$

At a specific rotation phase Φ , one first obtains the angle Θ . Then the ranges of θ_h and ϕ_h are determined by Θ and the opening angle ρ . The dependence of θ_h has been transformed into that of θ_{em} by the relation in Eq. (73). Finally, the observed spectral flux for a given mode is given by Eq. (75). Note that the integration domain is restricted to the hot region with the intensities being zero outside the hot region. The observed spectral flux F_I , F_Q , and F_U that are associated with the Stokes parameters I , Q , and U are (van Adelsberg & Lai 2006; van Adelsberg & Perna 2009)

$$F_I = F_O + F_X, \quad (76)$$

$$F_Q = F_I \Pi_{\text{em}} \cos 2\Psi(r_{\text{pl}}), \quad (77)$$

$$F_U = F_I \Pi_{\text{em}} \sin 2\Psi(r_{\text{pl}}), \quad (78)$$

and the observed polarization fraction is

$$\Pi_L = \frac{(F_Q^2 + F_U^2)^{1/2}}{F_I} = |\Pi_{\text{em}}|. \quad (79)$$

The observed polarization fraction is equal to the intrinsic polarization fraction, which arises from the assumption that the magnetic field is constant across the hot region which is much smaller than the surface area of the star.

We give an example with a magnetic field $B = 10^{14}$ G, an effective temperature $T_{\text{eff}} = 5 \times 10^6$ K, and a surface gravity $g = GM/R^2 \left(1 - 2GM/R/c^2\right)^{-1/2} = 2.4 \times 10^{14} \text{ cm s}^{-2}$ in Fig. 12. The normalized F_I , F_Q/F_I , and F_U/F_I for different photon energies are shown. There are distinctive features that reflect the interplay

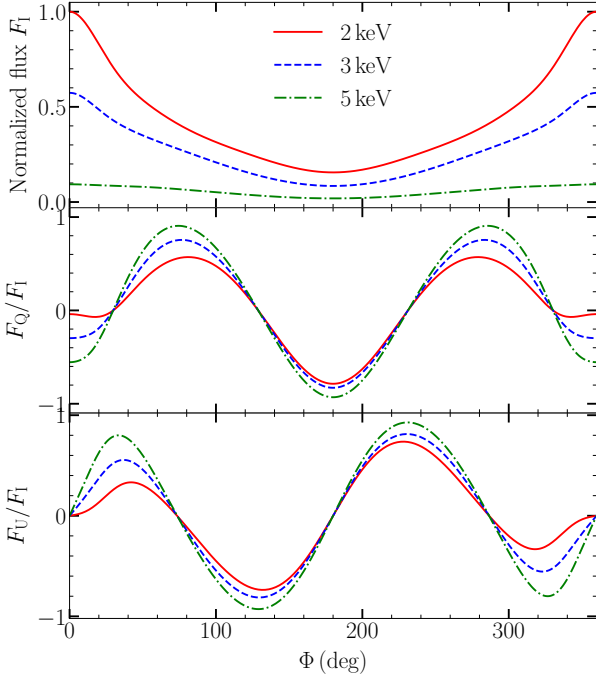


Figure 12. The phase evolutions of the spectral flux F_I (upper), the linear polarization F_Q/F_I (middle), and the linear polarization F_U/F_I (lower) for photon energies $E = 2$ keV, 3 keV, and 5 keV. The parameters of the model are the opening angle of the polar cap, $\rho = 5^\circ$, the dipole magnetic field $B = 10^{14}$ G, the effective temperature $T_{\text{eff}} = 5 \times 10^6$ K, the inclination angle of the observer $\iota = 45^\circ$, and the magnetic inclination angle $\alpha = 65^\circ$.

between the NS geometry, the strong magnetic field, and vacuum birefringence. Because the magnetic field $B > B_l \approx 7 \times 10^{13}$ G, the vacuum resonance density lies between the decoupling densities of the X mode and O mode photons ($\rho_O < \rho_V < \rho_X$), the linear polarization F_Q/F_I for different photon energies coincides in phase as the star rotates (van Adelsberg & Lai 2006).

The emergent radiation is dominated by the X mode except for θ_{em} close to zero. The polarization degree Π_L is smaller when the rotation phase Φ is close to 0 than for when it is close to 90° . This can be understood by considering the variation in X and O mode opacities when varying the angle between the photon propagation and magnetic field directions. In our chosen NS geometry, the emission angle θ_{em} is closer to zero for a rotation phase around $\sim 0^\circ$ compared to other phases. The difference between the X and the O mode opacities becomes smaller. Thus, the polarization fraction is smaller than at other phases. In contrast, the emission angle θ_{em} is close to $\sim 45^\circ$ when the rotation phase is far away from 0° or 360° . At those angles, the difference between the X and O mode opacities is maximal and the polarization fraction is larger.

5.2 Modulations on the Stokes parameters of X-rays

Since the phase evolution of the Stokes parameters are similar for different energies in Fig. 12, we fix $E = 3$ keV to study the modulations due to the precession. In Fig. 13, we show the phase evolution of the normalized F_I , F_Q/F_I , and F_U/F_I at different precession phases for a biaxial NS. Only half of the precession period is shown because the precession is periodic. The modulations for the triaxial case are similar. The precession mainly causes variations at a rotation phase close to 0° .

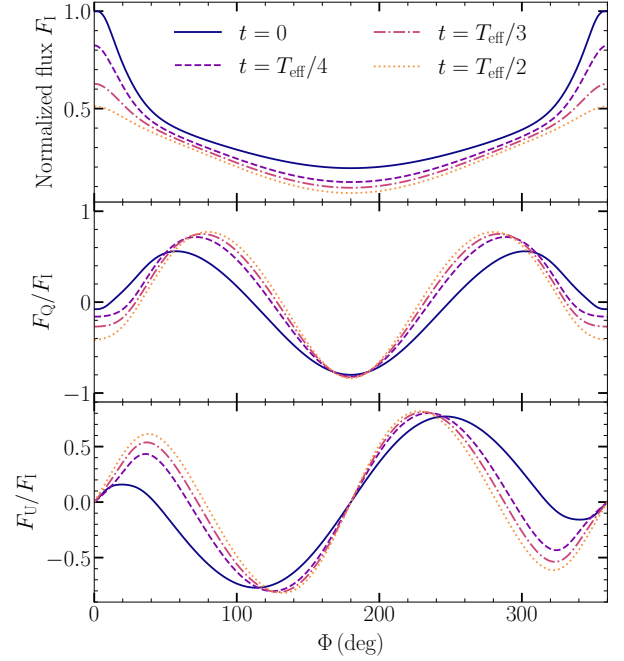


Figure 13. The phase-resolved spectral flux F_I (upper), F_Q/F_I (middle), and F_U/F_I (lower) of $E = 3$ keV at different precession phases for a biaxial NS. The parameters are shown in Case I of Table 3.

The phase-resolved X-ray polarization is usually hard to get from observations. Thus, we give the phase-averaged Stokes parameters $\langle F_I \rangle$, $\langle F_Q \rangle / \langle F_I \rangle$ and polarization degree $\langle \Pi_L \rangle$ in Fig. 14. The phase averaged F_U is zero and it is omitted in the figure. Both biaxial and triaxial cases are shown and the phase-averaged spectral flux $\langle F_I \rangle$ is normalized to the maximal value.

The amplitude of $\langle F_I \rangle / \langle F_I^{\text{max}} \rangle$ can vary up to $\sim 40\%$ during the precession, which is quite substantial. Heyl & Hernquist (2002) used free precession to explain the flux variations from the magnetar 1E 161348–5055. They modeled the hotspot emission in a similar way to our work. The large variations of the phase-averaged flux are partially caused by the emission model. We assume that the emission comes from a small hot region centered around the magnetic axis. If the emission comes from different patches or even the whole stellar surface with temperature profiles, the large modulations on the spectral flux might be reduced.

The phase-averaged linear polarization $\langle F_Q \rangle / \langle F_I \rangle$ and the phase-averaged polarization fraction $\langle \Pi_L \rangle$ vary $\sim 10\%$ – 20% in our examples. Different from the spectral flux, the modulations on the polarizations may not be reduced if the emission comes from different patches of the stellar surface. As we discussed before, when an X-ray photon propagates in the magnetosphere, its polarization state evolves adiabatically along the varying magnetic field up to the polarization limiting radius r_{pl} , which is far from the surface of the NS. Polarization states of photons from different patches of the star largely do not cancel. The magnetic field direction at r_{pl} changes during the precession and the modulations should always exist.

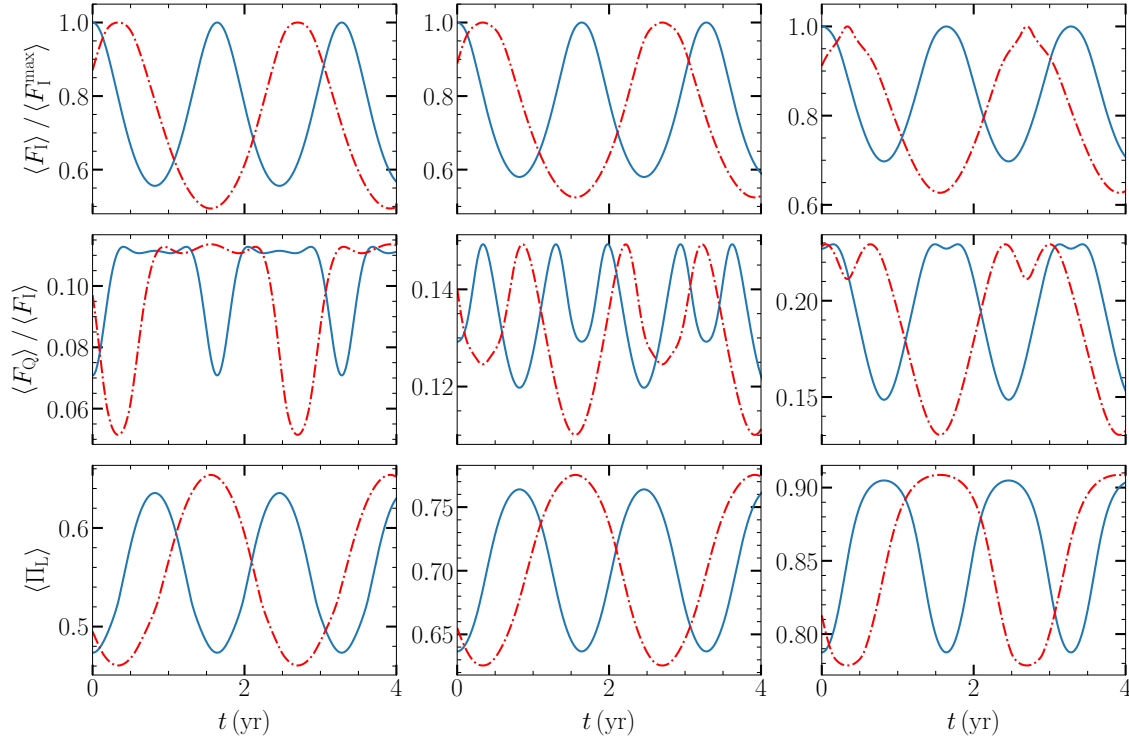
5.3 Modulations on polarized radio emission

We use the RVM to study the modulations on the polarized radio emission. It may be possible to observe the swing of the emission region and the modulations on the PA due to the precession.

We present the PA evolutions at different precession phases for a

Table 3. The intrinsic and effective parameters for modulated polarizations of X-rays and radio signals shown in Fig. 13-17.

| Case | Intrinsic parameters | | | | | | | | Effective parameters | | | | | |
|------|----------------------|--------------------|------------|----------|-------------------------|---------------------|---------------------|----------------------|-------------------------|-----------------------|--------------------------------------|----------------------------------|----------------------------------|-----------------------|
| | P_0 (s) | B (G) | ϵ | δ | θ_0 ($^\circ$) | χ ($^\circ$) | η ($^\circ$) | ι ($^\circ$) | ϵ_{eff} | δ_{eff} | $\theta_{\text{eff},0}$ ($^\circ$) | χ_{eff} ($^\circ$) | η_{eff} ($^\circ$) | T_{eff} (yr) |
| I | 5 | 10^{14} | 10^{-7} | 0 | 15 | 65 | 0 | 45 | 1.01×10^{-7} | 0.0124 | 15.3 | 65.3 | 0 | 1.64 |
| II | 5 | 10^{14} | 10^{-7} | 1 | 15 | 65 | 45 | 45 | 1.00×10^{-7} | 0.993 | 15.2 | 65.5 | 44.4 | 2.35 |
| III | 5 | 10^{14} | 10^{-7} | 0 | 15 | 45 | 0 | 45 | 1.00×10^{-7} | 0.00761 | 15.4 | 45.4 | 0 | 1.65 |
| IV | 5 | 10^{14} | 10^{-7} | 1 | 15 | 45 | 45 | 45 | 9.96×10^{-8} | 1.01 | 15.3 | 45.6 | 44.8 | 2.38 |
| V | 5 | 5×10^{14} | 10^{-7} | 0 | 15 | 45 | 0 | 45 | 1.07×10^{-7} | 0.261 | 25.3 | 55.3 | 0 | 1.87 |
| VI | 5 | 5×10^{14} | 10^{-7} | 1 | 15 | 45 | 45 | 45 | 9.99×10^{-8} | 1.15 | 24.9 | 60.2 | 36.1 | 2.75 |
| VII | 5 | 10^{14} | 10^{-5} | 0 | 18 | 40 | 0 | 45 | 1.00×10^{-5} | 6.20×10^{-5} | 18.0 | 40.0 | 0 | 0.0167 |
| VIII | 5 | 10^{14} | 10^{-5} | 5 | 18 | 40 | 0 | 45 | 1.00×10^{-5} | 5.00 | 18.0 | 40.0 | 0 | 0.0490 |


Figure 14. The time evolutions of the phase-averaged normalized spectral flux $\langle F_I \rangle / \langle F_I^{\text{max}} \rangle$ (upper), the phase-averaged linear polarization $\langle F_Q \rangle / \langle F_I \rangle$ (middle), and the phase-averaged polarization fraction $\langle \Pi_L \rangle$ (lower) for photon energies $E = 2$ keV (left), $E = 3$ keV (middle) and $E = 5$ keV (right). The parameters for the biaxial and triaxial cases are shown in Case I and Case II of Table 3 respectively.

magnetar with $B = 10^{14}$ G in the upper panel of Fig. 15. Due to the precession, the slope of the PA will change. The steepest gradient of the PA is

$$\left. \frac{d\Psi}{d\Phi} \right|_{\Phi=0} = -\frac{\sin \alpha}{\sin \beta}. \quad (80)$$

Practically, the precession of magnetars may be observed from the variations of the steepest gradient of the PA. As we take the inclination angle of the observer to be $\iota = \pi/4$, the impact parameter $\beta = \iota - \alpha$ changes sign during precession. Thus the slope of the PA can potentially change sign. In the lower panel of Fig. 15, we show the inverse of the steepest gradient, $-\sin \beta / \sin \alpha$ for a better illustration.

For comparison, we also give examples with $B = 5 \times 10^{14}$ G in Fig. 16. The effects of the near-field torque cannot be neglected. The wobble angle varies across a much larger range and the modulations of the steepest gradient are distinct from that in Fig. 15. Moreover, the

differences between the biaxial and triaxial cases are more obvious than Fig. 15.

The parameter m is on the order of 0.1 for the examples shown in Table 3. As shown in the lower panels of Fig. 15 and Fig. 16, the modulations for the biaxial and triaxial cases are similar. In contrast, the triaxiality can be observed directly from polarizations if m is large enough. We show a triaxial case with $m = 0.528$ in Fig. 17. For the biaxial case, the wobble angle is constant, the variation of α and $-\sin \beta / \sin \alpha$ is harmonic and has only one peak. In fact, these features are true for any biaxial case according to Eq. (41). For the triaxial case, the modulations of α and $-\sin \beta / \sin \alpha$ are not harmonic. Due to the variation of the wobble angle, the time evolution of α and $-\sin \beta / \sin \alpha$ also shows a “double-peak” structure in our case.

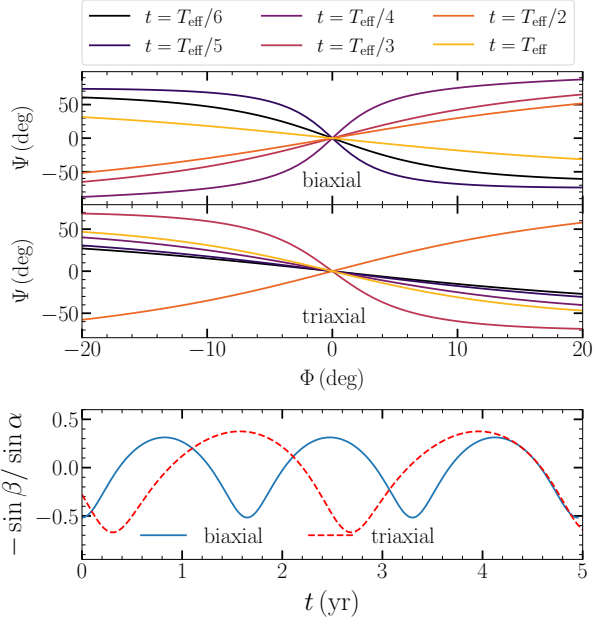


Figure 15. The upper panel shows the PA evolution at different precession phases for both biaxial and triaxial cases. The lower panel shows the time evolution of the inverse of the steepest gradient, $-\sin \beta / \sin \alpha$. The parameters for the biaxial and triaxial cases are shown in Case III and Case IV of Table 3 respectively.

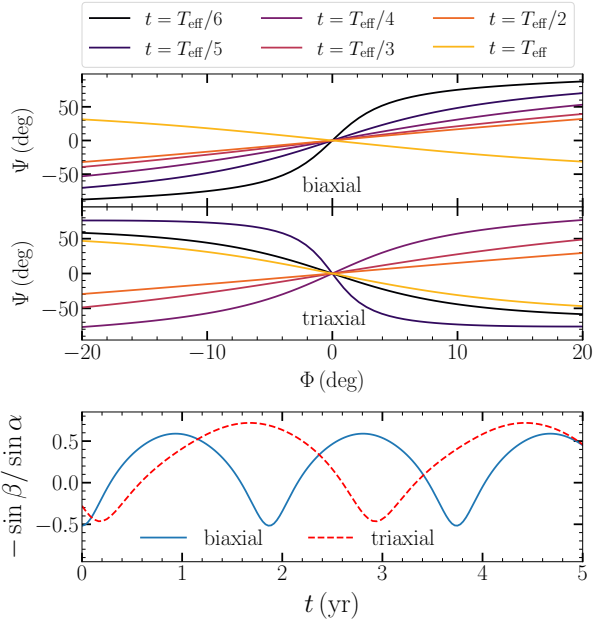


Figure 16. Same as Fig. 15 but with a larger magnetic field $B = 5 \times 10^{14}$ G. The parameters for the biaxial and triaxial cases are shown in Case V and Case VI of Table 3 respectively.

6 DISCUSSIONS

In our work, we gave the analytical solutions to the free precession of triaxially-deformed NSs following Landau & Lifshitz (1960), Akgun et al. (2006), and Wasserman et al. (2022). We assumed that the rotation is rigid and ignored superfluid pinning or any internal dissipations. The pinning of the superfluid can lead to fast precession

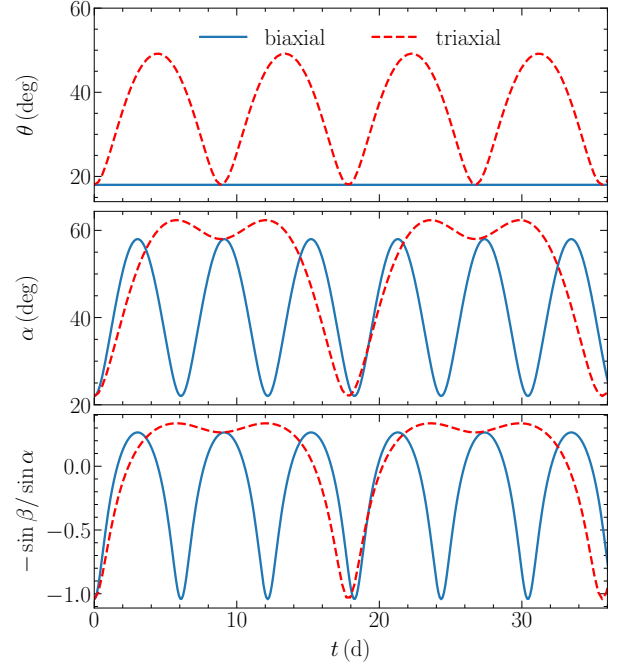


Figure 17. The time evolution of θ , α , and $-\sin \beta / \sin \alpha$. The parameters for the biaxial and triaxial cases are shown in Case VII and Case VIII of Table 3 respectively.

comparable to the spin frequency (Shaham 1977; Sedrakian et al. 1998). It is also possible that the precession is damped quickly by the coupling of normal fluids to the superfluid core if the strong internal magnetic field of magnetars unpairs the proton superconductor in the stellar core (Sedrakian 2016). In this regard, our studies can serve as a starting point to further investigate the internal couplings and dissipative mechanisms.

The strong magnetic fields of magnetars also induce large electromagnetic torques, which are important to determine the spin and geometry evolutions of precessing magnetars. Assuming a dipole field, we considered both the near-field and far-field electromagnetic torques in the forced precession problem.

For magnetars with large external magnetic fields, the near-field torque couples to the precession solution and affects the motions substantially. This is the central idea in the so called radiative precession advocated by Melatos (1997, 2000). The near-field torque can be effectively absorbed into the moment of inertia tensor of the star (Melatos 2000; Glampedakis & Jones 2010; Zanazzi & Lai 2015). We solved the forced precession problem analytically by transforming the near-field torque into an effective deformation along the magnetic axis. We found that the effects of the near-field torque cannot be ignored in the dynamical evolution if $\epsilon_m \geq 0.1\epsilon$, where ϵ_m is the effective ellipticity induced by the external magnetic field and ϵ is the ellipticity sourced from the magnetic and elastic deformations.

The far-field torque leads to the spin down and secular change of the magnetic inclination angle. Perturbation methods were used to study the forced precession under the far-field torque. We obtained analytical solutions of the spin evolution for general triaxial stars. One part of the far-field torque comes from the direct emission of electromagnetic waves due to the time-varying magnetic multipolar moments of the star. Another part is caused by electromagnetic emission from charged particles being accelerated in the magnetosphere. Therefore, we not only used the simple vacuum torque, but also applied a parametrized plasma-filled torque proposed by Li et al.

(2012) and Philippov et al. (2014) according to MHD simulations. The form of the plasma-filled torque is equivalent to adding an alignment component of the far-field torque compared to the vacuum case. Note that the near-field torque affects the spin-down rate indirectly because it leads to the variations of the magnetic inclination angle for a precessing magnetar.

In our calculations, we assumed that the external magnetic field was dipolar. It is commonly believed that higher multipoles should be considered crucially for magnetars. Zanazzi & Lai (2015) investigated the near-field torque contributed by the quadrupole field. The effective deformation is not symmetric about a specific axis and can be classified into two independent components. The multipoles contributing to the near-field torque can also be absorbed into the moment of inertia tensor of the star. The solutions in our work can still be applied but with different effective parameters. The direct electromagnetic emission from the magnetic multipoles is probably dominated by the magnetic dipole. On the perspective of observations, we may leave the coefficients in the parametrized far-field torque in Eq. (20) as free parameters to absorb the effects of higher magnetic multipoles, as well as complex charges and currents in the magnetosphere.

During the precession, the torques are locked in phase with the precession, which in turn modulates the spin-down rate. We first studied the spin evolution of triaxially-deformed magnetars and gave the analytical timing residuals, which contained the geometric term resulting from the phase modulations of the precession and the spin-down term arising from the varying far-field torque.

The polarization maps out the geometry of the emission region and can serve as a useful probe to find the precession of magnetars. For the soft X-rays, we used the model given in Lai & Ho (2003) and van Adelsberg & Lai (2006) to calculate the observed Stokes parameters emitted from a hot region centered around the magnetic dipole. The general relativistic effects and the vacuum birefringence were considered. We investigated the modulations on the spectral intensities, the linear polarization, and the polarization fraction for both phase-resolved and phase-averaged scenarios. For radio signals, we simply used the RVM to study the PA evolution for different geometries during the precession. It is possible to detect the precession of transient magnetars through the variations of the steepest gradient of the PA if large-amplitude precession is excited.

The polarization state of X-rays evolves adiabatically following the varying magnetic field it experiences up to the polarization limiting radius r_{pl} . The polarization states of photons from different patches of the star tend to align at r_{pl} , and largely do not cancel (Heyl et al. 2003; Lai & Ho 2003). Therefore, the polarizations can still be modulated in the precession, even when the photons come from different patches (or even the whole stellar surface) because the inclination of the magnetic field at r_{pl} changes. In contrast, the modulations of the flux and the spectrum may be reduced or even eliminated if the emission comes from a large extended region.

From the perspective of observations, IXPE has conducted the first observation of the polarized X-ray emissions from the magnetar 4U 0142+61 (Taverna et al. 2022). In near future, the eXTP mission will give more accurate measurements of X-ray polarizations (Zhang et al. 2019; in 't Zand et al. 2019) which will give us more opportunities to find the precession of magnetars via polarizations.

7 CONCLUSIONS

We gave a detailed model of precessing magnetars with triaxial deformation. The dynamical motion of the precession both in free

and forced conditions was studied analytically. For magnetars with $B \sim 5 \times 10^{14} - 10^{15}$ G, the effects of the electromagnetic torques must be considered crucially if the ellipticity $\epsilon \lesssim 10^{-7}$.

Precession can produce observational consequences in timing and polarization. We gave the timing residuals from both the geometric term arising from the precession and the spin-down term arising from the variations of the far-field torque. The relative strength of the two terms is determined by the relative strength between the rotation period P , the precession timescale τ_p , and the spin-down timescale τ_{rad} . If $\tau_p/\tau_{rad} \gg P/\tau_p$, the spin-down term dominates. Otherwise, the geometric term dominates over the spin-down term.

We also modeled the modulations on polarized X-ray and radio signals in different NS geometries. Assuming the emission is centered around one of the magnetic pole, we showed that the prospects of detecting precession with polarization are promising if large wobble angle is excited. Thanks to the QED effects in strongly magnetized magnetosphere, the modulations on the polarization of X-rays may always exist even if the emission comes from a much extended region or the whole star. Advanced detectors, such as IXPE and eXTP, will give us more opportunities to find the precession of magnetars via polarizations.

A firm detection of magnetar precession will answer many questions about the strong internal magnetic field, the emission geometry, and the equation of state of NSs. Our timing and polarization models can be used to search and interpret magnetar precession.

In this work, we assume that the emission comes from a small region centered around the magnetic pole and the magnetic field itself is dipolar. However, the emission may come from a much extended region and possibly is distorted by the scattering processes (Caiazzo et al. 2022) for magnetars. The actual magnetic structures of magnetars are likely to have a twisted magnetic field configuration which contains contributions from higher-order multipoles, affecting the polarization-state evolution for both radio signals from transient magnetars (Tong et al. 2021) and X-rays (Fernandez & Davis 2011; Taverna et al. 2015). We leave the modelling of the polarized X-rays and radio emission from precessing magnetars with more complex emission mechanisms and magnetic fields into future studies.

ACKNOWLEDGEMENTS

We thank Kuo Liu for carefully reading the manuscript, and Jingyuan Deng, Zexin Hu, and Rui Xu for discussions. This work was supported by the National SKA Program of China (2020SKA0120300), the National Natural Science Foundation of China (11975027, 11991053, 11721303), the Max Planck Partner Group Program funded by the Max Planck Society, and the High-performance Computing Platform of Peking University. DJJ acknowledges support from the STFC via grant number ST/R00045X/1.

DATA AVAILABILITY

The data underlying this paper will be shared on reasonable request to the corresponding authors.

REFERENCES

- Akgun T., Wasserman I., 2008, *MNRAS*, 383, 1551
- Akgun T., Link B., Wasserman I., 2006, *MNRAS*, 365, 653
- Arzamasskiy L., Philippov A., Tchekhovskoy A., 2015, *MNRAS*, 453, 3540
- Ashton G., Jones D. I., Prix R., 2016, *MNRAS*, 458, 881

- Ashton G., Jones D., Prix R., 2017, *MNRAS*, 467, 164
- Beloborodov A. M., 2002, *ApJL*, 566, L85
- Beskin V. S., Zheltoukhov A. A., 2014, *Phys. Usp.*, 57, 799
- Beskin V. S., Zheltoukhov A. A., Obukhova A. K., Stroinov E. E., 2013, *Bull. Lebedev Phys. Inst.*, 40, 265
- Braithwaite J., 2009, *MNRAS*, 397, 763
- Caiazzo I., González-Caniulef D., Heyl J., Fernández R., 2022, *MNRAS*, 514, 5024
- Camilo F., Ransom S., Halpern J., Reynolds J., Helfand D., Zimmerman N., Sarkissian J., 2006, *Nature*, 442, 892
- Camilo F., Ransom S. M., Halpern J. P., Reynolds J., 2007, *ApJL*, 666, L93
- Cioffi R., Ferrari V., Gualtieri L., 2010, *MNRAS*, 406, 2540
- Cutler C., Jones D. I., 2001, *Phys. Rev. D*, 63, 024002
- Cutler C., Ushomirsky G., Link B., 2003, *ApJ*, 588, 975
- Davis L., Goldstein M., 1970, *ApJ*, 159, L81
- Deutsch A. J., 1955, *Annales d'Astrophysique*, 18, 1
- Eatough R. P., et al., 2013, *Nature*, 501, 391
- Fernandez R., Davis S. W., 2011, *ApJ*, 730, 131
- Gao Y., Shao L., Xu R., Sun L., Liu C., Xu R.-X., 2020, *MNRAS*, 498, 1826
- Gittins F., Andersson N., Jones D. I., 2020, *MNRAS*, 500, 5570
- Glampedakis K., Jones D. I., 2010, *MNRAS*, 405, L6
- Glampedakis K., Lasky P. D., 2016, *MNRAS*, 463, 2542
- Glampedakis K., Andersson N., Jones D. I., 2008, *Phys. Rev. Lett.*, 100, 081101
- Gnedin I. N., Sunyaev R. A., 1974, *A&A*, 36, 379
- Goldreich P., 1970, *ApJL*, 160, L11
- Good M. L., Ng K. K., 1985, *ApJ*, 299, 706
- Haskell B., Jones D. I., Andersson N., 2006, *MNRAS*, 373, 1423
- Haskell B., Samuelsson L., Glampedakis K., Andersson N., 2008, *MNRAS*, 385, 531
- Heisenberg W., Euler H., 1936, *Z. Phys.*, 98, 714
- Heyl J. S., Hernquist L., 2002, *ApJ*, 567, 510
- Heyl J. S., Shaviv N. J., Lloyd D., 2003, *MNRAS*, 342, 134
- Ho W. C. G., Lai D., 2001, *MNRAS*, 327, 1081
- Ho W. C. G., Lai D., 2003, *MNRAS*, 338, 233
- Horowitz C. J., Kadau K., 2009, *Phys. Rev. Lett.*, 102, 191102
- Johnson-McDaniel N. K., Owen B. J., 2013, *Phys. Rev. D*, 88, 044004
- Jones D. I., 2012, *MNRAS*, 420, 2325
- Jones D. I., Andersson N., 2001, *MNRAS*, 324, 811
- Kaspi V. M., Beloborodov A., 2017, *ARA&A*, 55, 261
- Kaspi V. M., Chakrabarty D., Steinberger J., 1999, *ApJL*, 525, L33
- Kaspi V. M., Gavriil F. P., Chakrabarty D., Lackey J. R., Muno M. P., 2001, *ApJ*, 558, 253
- Kramer M., Lyne A. G., O'Brien J. T., Jordan C. A., Lorimer D. R., 2006, *Science*, 312, 549
- Kramer M., Stappers B. W., Jessner A., Lyne A. G., Jordan C. A., 2007, *MNRAS*, 377, 107
- Lai D., Ho W. C. G., 2003, *Phys. Rev. Lett.*, 91, 071101
- Landau L. D., Lifshitz E. M., 1960, *Mechanics*. Oxford
- Lander S. K., 2013, *Phys. Rev. Lett.*, 110, 071101
- Lander S. K., Jones D. I., 2009, *MNRAS*, 395, 2162
- Lander S. K., Jones D. I., 2012, *MNRAS*, 424, 482
- Lander S. K., Jones D. I., 2017, *MNRAS*, 467, 4343
- Lander S. K., Jones D. I., 2018, *MNRAS*, 481, 4169
- Lander S. K., Jones D. I., 2020, *MNRAS*, 494, 4838
- Lasky P. D., Melatos A., 2013, *Phys. Rev. D*, 88, 103005
- Levin L., et al., 2010, *ApJL*, 721, L33
- Levin L., et al., 2012, *MNRAS*, 422, 2489
- Levin Y., Beloborodov A. M., Bransgrove A., 2020, *ApJL*, 895, L30
- Li J., Spitkovsky A., Tchekhovskoy A., 2012, *ApJ*, 746, 60
- Link B., 2007, *Ap&SS*, 308, 435
- Link B., Epstein R. I., 2001, *ApJ*, 556, 392
- Lorimer D. R., Kramer M., 2005, *Handbook of Pulsar Astronomy*. Cambridge University Press, Cambridge, England
- Lower M. E., Shannon R. M., Johnston S., Bailes M., 2020, *ApJL*, 896, L37
- Lower M. E., Johnston S., Shannon R. M., Bailes M., Camilo F., 2021, *MNRAS*, 502, 127
- Lyne A., Hobbs G., Kramer M., Stairs I., Stappers B., 2010, *Science*, 329, 408
- Makishima K., 2016, *Proceedings of the Japan Academy, Series B*, 92, 135
- Makishima K., Enoto T., Hiraga J. S., Nakano T., Nakazawa K., Sakurai S., Sasano M., Murakami H., 2014, *Phys. Rev. Lett.*, 112, 171102
- Makishima K., Enoto T., Yoneda H., Odaka H., 2021a, *MNRAS*, 502, 2266
- Makishima K., Tamba T., Aizawa Y., Odaka H., Yoneda H., Enoto T., Suzuki H., 2021b, *ApJ*, 923, 63
- Mastrano A., Lasky P. D., Melatos A., 2013, *MNRAS*, 434, 1658
- Mastrano A., Suvorov A. G., Melatos A., 2015, *MNRAS*, 447, 3475
- Melatos A., 1997, *MNRAS*, 288, 1049
- Melatos A., 2000, *MNRAS*, 313, 217
- Mestel L., Takhar H. S., 1972, *MNRAS*, 156, 419
- Meszáros P., 1992, *High-energy radiation from magnetized neutron stars*. University of Chicago Press
- Meszáros P., Novick R., Szentgyorgyi A., Chanan G. A., Weisskopf M. C., 1988, *ApJ*, 324, 1056
- Morales J. A., Horowitz C. J., 2022, *MNRAS*, 517, 5610
- Olausen S. A., Kaspi V. M., 2014, *ApJS*, 212, 6
- Page D., 1995, *ApJ*, 442, 273
- Pavlov G. G., Zavlin V. E., 2000, *ApJ*, 529, 1011
- Pechenick K. R., Ftaclas C., Cohen J. M., 1983, *ApJ*, 274, 846
- Philippov A., Tchekhovskoy A., Li J. G., 2014, *MNRAS*, 441, 1879
- Pines D., 1974, *Nature*, 248, 483
- Radhakrishnan V., Cooke D. J., 1969, *Astrophys. Lett.*, 3, 225
- Sedrakian A., 2016, *A&A*, 587, L2
- Sedrakian A., Wasserman I., Cordes J. M., 1998, *ApJ*, 524, 341
- Shaham J., 1977, *ApJ*, 214, 251
- Shaw B., et al., 2022, *MNRAS*, 513, 5861
- Stairs I. H., Lyne A. G., Shemar S. L., 2000, *Nature*, 406, 484
- Stairs I. H., et al., 2019, *MNRAS*, 485, 3230
- Taverna R., Turolla R., Caniulef D. G., Zane S., Muleri F., Soffitta P., 2015, *MNRAS*, 454, 3254
- Taverna R., et al., 2022, *Science*, 378, 646
- Thompson C., Lyutikov M., Kulkarni S. R., 2002, *ApJ*, 574, 332
- Tong H., Wang P. F., Wang H. G., Yan Z., 2021, *MNRAS*, 502, 1549
- Tsai W. Y., Erber T., 1975, *Phys. Rev. D*, 12, 1132
- Turolla R., Zane S., Watts A., 2015, *Rept. Prog. Phys.*, 78, 116901
- Ushomirsky G., Cutler C., Bildsten L., 2000, *MNRAS*, 319, 902
- Wasserman I., 2003, *MNRAS*, 341, 1020
- Wasserman I., Cordes J. M., Chatterjee S., Batra G., 2022, *ApJ*, 928, 53
- Zanazzi J., Lai D., 2015, *MNRAS*, 451, 695
- Zanazzi J. J., Lai D., 2020, *ApJ*, 892, L15
- Zhang S.-N., et al., 2019, *Sci. China Phys. Mech. Astron.*, 62, 29502
- in 't Zand J. J. M., et al., 2019, *Sci. China Phys. Mech. Astron.*, 62, 029506
- van Adelsberg M., Lai D., 2006, *MNRAS*, 373, 1495
- van Adelsberg M., Perna R., 2009, *MNRAS*, 399, 1523

APPENDIX A: JACOBI ELLIPTIC FUNCTIONS

The Jacobi elliptic functions are standard forms of elliptic functions. The three basic functions are denoted as $\text{cn}(\tau, m)$, $\text{sn}(\tau, m)$, and $\text{dn}(\tau, m)$, where $0 \leq m \leq 1$. They naturally arise from the following integral

$$\tau = \int_0^s \frac{dt}{\sqrt{1 - m \sin^2 t}}, \quad (\text{A1})$$

where $s = \text{am}(\tau, m)$ is called the Jacobi amplitude. Then, it follows

$$\begin{aligned} \cos s &= \text{cn}(\tau, m), \\ \sin s &= \text{sn}(\tau, m), \\ \sqrt{1 - m \sin^2 s} &= \text{dn}(\tau, m). \end{aligned} \quad (\text{A2})$$

The Jacobi elliptic functions are periodic with period $T = 4K(m)$, where $K(m)$ is the complete elliptic integral of the first kind.

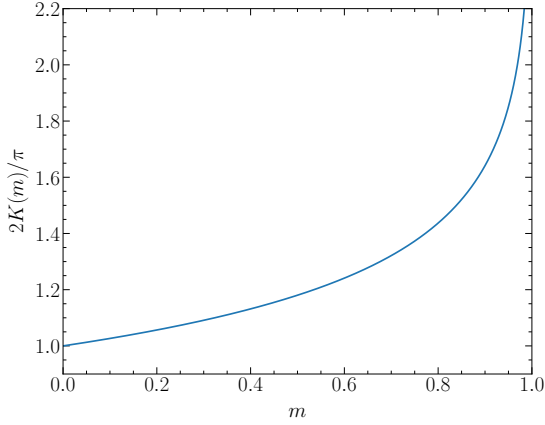


Figure A1. The relation between m and $2K(m)/\pi$.

The expansions of the Jacobi elliptic function in series of m are

$$\begin{aligned} \text{cn}(\tau, m) &= \cos \tau - \frac{1}{8}m \sin \tau (-2\tau + \sin 2\tau) + O(m^2), \\ \text{sn}(\tau, m) &= \sin \tau + \frac{1}{8}m \cos \tau (-2\tau + \sin 2\tau) + O(m^2), \\ \text{dn}(\tau, m) &= 1 - \frac{1}{2}m \sin^2 \tau + O(m^2). \end{aligned} \quad (\text{A3})$$

When $m = 0$, $K(0) = \pi/2$, the variable τ equals to the Jacobi amplitude s , and the three elliptic functions turn into

$$\begin{aligned} \text{cn}(\tau, 0) &= \cos \tau, \\ \text{sn}(\tau, 0) &= \sin \tau, \\ \text{dn}(\tau, 0) &= 1. \end{aligned} \quad (\text{A4})$$

The trigonometric functions are 2π periodic. In Fig. A1, we show the relation between the parameter m and the period of the Jacobi elliptic functions over the period of the trigonometric functions.

The quantity $\cos \alpha$ shown in Eq. (40) is a function of the Jacobi elliptic functions. The integration of $\cos^2 \alpha$ is

$$\begin{aligned} \int_0^t \cos^2 \alpha dt &= \frac{\cos^2 \theta_0}{\omega_p \delta} \left[\hat{\mu}_1^2 - (1 + \delta) \hat{\mu}_2^2 + \hat{\mu}_3^2 \delta \right] E(\text{am } \tau) \\ &+ \frac{1}{\omega_p} \left[-\sin 2\theta_0 (1 + \delta)^{\frac{1}{2}} \hat{\mu}_2 \hat{\mu}_3 \text{cn } \tau \right] \\ &+ \frac{1}{\omega_p} \sin 2\theta_0 \hat{\mu}_1 \hat{\mu}_3 \text{sn} \\ &+ \frac{\cos^2 \theta_0}{\delta \omega_p} \left[(-1 + \delta \tan^2 \theta_0) \hat{\mu}_1^2 + (1 + \delta) \hat{\mu}_2^2 \right] \tau \\ &- \frac{2 \cos^2 \theta_0 \hat{\mu}_1 \hat{\mu}_2 (1 + \delta)^{\frac{1}{2}}}{\omega_p \delta} \text{dn } \tau + A_c, \end{aligned} \quad (\text{A5})$$

where $E(\text{am } \tau)$ is the Jacobi elliptic integral of the second kind, and $\text{am } \tau = \arcsin(\text{sn } \tau)$ is the Jacobi amplitude. The term A_c is an integration constant, which can be obtained directly by setting the integral to be zero at the initial time $t = 0$.

This paper has been typeset from a \LaTeX file prepared by the author.